Rai, Ranjodh, Ma, Zhihua ORCID logoORCID: https://orcid.org/0000-0002-2426-3038, Lin, Zaibin, Bai, Wei ORCID logoORCID: https://orcid.org/0000-0002-3537-207X and Qian, Ling ORCID logoORCID: https://orcid.org/0000-0002-9716-2342 (2023) A stable free-surface boundary solution method for fully nonlinear potential flow models. Applied Ocean Research, 134. p. 103500. ISSN 0141-1187

A stable free-surface boundary solution method for fully nonlinear potential flow models

Ranjodh Rai [a], Zhihua Ma [a],[*], Zaibin Lin [a,b], Wei Bai [a], Ling Qian [a]

[a] *Manchester Metropolitan University, Chester Street, Manchester, M1 5GD, United Kingdom*
[b] *School of Engineering, University of Aberdeen, Aberdeen, AB24 3UE, United Kingdom*

ARTICLE INFO

ABSTRACT

This paper presents a stable method for solving the kinematic boundary condition equation (KBC) in fully nonlinear potential flow (FNPF) models. The method is motivated by a total variation diminishing (TVD) approach, which makes it especially applicable to advection-dominated partial differential equations such as the KBC. It is also simple, and can be easily implemented in existing finite volume-based FNPF models for wave hydrodynamics. The method is systematically assessed through a series of test cases: the propagation of second and fifth-order Stokes waves; focused wave propagation; and wave shoaling in both 2 and 3-D. It was found that the method stabilised the computation in every instance: it successfully eliminated the sawtooth instability, which commonly arises in FNPF models, without a reduction in computational efficiency. Consequently, we avoided the use of undesirable stabilisation techniques that involve artificial dissipation such as low-order smoothing. The method is also accurate: it produced satisfactory numerical solutions that agreed well with experimental, analytical and other published numerical results. It was also found that the method is superior than classical schemes in terms of energy conservation, applicability, and efficiency—all salient features that are essential for large-scale and long-time simulations.

1. Introduction

For a number of decades now, a versatile numerical hydrodynamic model – capable of accurately and efficiently simulating both wave–wave and wave–structure interactions – has long been sought after in environmental science and engineering. Traditionally, numerical models for wave hydrodynamics have largely been based on potential flow theory, with a lot of effort being devoted to the development of fully nonlinear potential flow (FNPF) models in particular. These types of models are advantageous in the fact that they are computationally efficient; simultaneously, these models provide sufficiently accurate solutions to a number of problems involving wave propagation and wave–wave interaction, applicable in marine areas spanning deep to shallow water. They can also be used for a number of wave–structure interaction problems, but the inability of these models to take into account viscosity, vorticity, and other important physical effects means that in recent years Navier–Stokes (NS) equations based computational fluid dynamics (CFD) models have gained popularity. However, these types of models are usually computationally expensive, so currently there is also a concerted effort to develop integrated (or hybrid) models that aim to utilise the advantages of both FNPF and NS models through some sort of coupling between each individual solver in a numerical

wave tank (NWT). This type of advanced integrated model evidently still needs a highly accurate and efficient FNPF solver as one of its constituent parts. Hence, improving existing FNPF models – or even developing new advanced FNPF models – which can then be used as component and/or standalone solvers is still of interest and great importance.

Customarily, FNPF models have been based predominantly on the boundary element method (BEM) (Kim et al., 1998; Grilli et al., 2001; Dold, 1992), finite element method (FEM) (Wu and Eatock Taylor, 1994; Ma et al., 2001a; Ma and Yan, 2006), or finite difference method (FDM) (Bihs et al., 2020; Li and Fleming, 1997; Engsig-Karup et al., 2009). However, more recent contributions have also been made using newer methods such as spectral (Ducrozet et al., 2016), spectral element (SE) (Engsig-Karup et al., 2016), and spectral boundary integral (SBI) (Fructus et al., 2005), as well as the finite volume method (FVM) (Lin et al., 2021). A more extensive review of these methods can be found in Lin et al. (2021). Naturally, each numerical method has its own advantages and disadvantages, but one problem that commonly arises in FNPF models – and has been extensively reported regardless of numerical method – is the so called 'sawtooth instability'. The consequence of this instability is that the free-surface boundary

---

develops a sawtooth like wave profile after some time, particularly when simulating steep waves. This instability was first observed by Longuet-Higgins and Cokelet (1976) in their seminal work where they also first outlined the mixed Eulerian–Lagrangian (MEL) approach— an approach which most proceeding FNPF models adopted. The direct source of this instability has not been definitively proven; few authors in the literature attempt to verify the source and instead elect only to mitigate the problem. However, Dias and Bridges (2006) suggested, 'The presence of sawtooth instabilities can be expected in the theory for nonlinear systems without dissipation, wherein energy flows from low to high wavenumbers and accumulates at the highest wavenumber associated with the discretisation'. This does not necessarily source the instability, but does suggest that it may be inherent in FNPF models, whilst also giving a basis from which mitigating measures can be developed. Dold (1992) also split the occurring instability into three types: weak, strong, and steep-wave. Through this he attempted to investigate how each type materialises, leading to suggestions of how each could be mitigated. Nevertheless, regardless of source, it is clear that some sort of stabilisation technique has to be utilised to ensure that any given model is free from the sawtooth instability.

By far the most popular technique in the literature for stabilising FNPF models is to use some form of numerical damping, such as smoothing. Indeed, as well as developing the MEL method, Longuet-Higgins and Cokelet (1976) also outlined a 5-point smoothing formula which has regularly been used by other authors such as Wu and Eatock Taylor (1994) and Mehmood et al. (2016). A variety of other damping techniques also exist, such as the fourth-order damping correction used by Lin et al. (2021) and the volume-conservative smoother proposed by Ferrand and Harris (2021). In general, smoothing is usually carried out on the free-surface variables η and ϕ – elevation and velocity potential respectively – in order to act as a form of artificial dissipation, just like the type described by Dias and Bridges (2006) previous. However, these sorts of artificial techniques – particularly the common lower order types mentioned – are not desirable because they can potentially cause superfluous dissipation, resulting in overall loss in energy in the system. This in turn can then make FNPF models inaccurate, particularly for large-scale and long-time simulations. Moreover, these techniques can involve a number of parameters that have to be tuned for any given application in order to achieve an optimal balance between stability and accuracy, resulting in a very sluggish and drawn-out process of trial and error if the values are not known a priori. However, it should also be noted that higher-order techniques formulated on large stencils, such as the original tenth-order 13-point Savitzky–Golay (S–G) filter (Savitzky and Golay, 1964) utilised by Engsig-Karup et al. (2009) and Hanssen et al. (2022), and improved S–G filters developed by Shao et al. (2022), can stabilise large-scale FNPF models with negligibly small energy loss for a number of applications. This is also without explicitly requiring tuning of any parameters like the lower-order filters.

Even though most FNPF models suffer from the sawtooth instability, subsequently requiring some form of numerical damping, there are examples of models that do not. For example, Grilli et al. (1989, 2001) developed a 2-D and 3-D model, both of which did not report the instability and hence required no smoothing or remeshing. The authors attributed the high accuracy and stability of the models to a unique high-order BEM method and a second-order Taylor series-based time-stepping scheme, further details of which can be found in Grilli et al. (2001). This Taylor series scheme was actually first utilised by Dold and Peregrine (1986), a model also based on the BEM. Again, the sawtooth instability did not appear, but only so long as a sufficiently small time step was adopted, a point Dold expands on in Dold (1992). However, in the latter article he also stated that for steep waves, the instability always appears when the simulation is allowed to continue over a sufficiently long period of time, and that smoothing is required in this situation. This indicates that Grilli et al. may be correct in their aspersion that it is a combination of factors that stabilised their models,

and that a high-order time-integration scheme in itself may not be sufficient.

In addition to the BEM models by Grilli et al. (1989, 2001), there are also examples of FEM models that do not suffer from the sawtooth instability and hence require no smoothing or remeshing. Early FEM models such as Wu and Eatock Taylor (1994) and Ma et al. (2001a,b) did require smoothing and remeshing respectively, but Ma and Yan later developed the quasi arbitrary Lagrangian–Eulerian finite element method (QALE-FEM) (Ma and Yan, 2006; Yan and Ma, 2007; Ma and Yan, 2009) which avoided the need for smoothing and remeshing. This is likely due to their precisely controlled mesh movement and highly accurate free-surface velocity calculation, aspects which some other FNPF models may under perform in. The finite difference-based FNPF model of Bihs et al. (2020) also avoided the explicit use of numerical damping. This model applied a second-order central difference (CD) scheme to discretise the σ-transformed Laplace equation, and a fifth-order weighted essentially non-oscillatory (WENO) scheme to discretise the convection terms in the free-surface boundary condition equations. Mola et al. (2013) used the stream-wise upwind Petrov–Galerkin scheme to remove the sawtooth instability. This was accomplished by introducing weighted projections in the free-surface boundary condition equations. Furthermore, spectral methods based models in the literature often attribute numerical instability to aliasing effects, hence usually some sort of anti-aliasing technique is utilised in order to mitigate these effects and any consequent numerical instability. For example, Fructus et al. (2005) produced a 3-D SBI model that used an anti-aliasing technique involving zeros-padding, meaning it therefore required no smoothing or remeshing, and importantly showed no signs of the sawtooth instability. However, there is an argument to suggest that some anti-aliasing techniques, such as the spectral filtering used by Engsig-Karup et al. (2016), are themselves a form of numerical damping as dissipation is being artificially added to the model.

Lin et al. (2021) recently developed a finite volume–based FNPF model within the framework of the open-source CFD software Open-FOAM. A key advantage of this model is that it is capable of dealing with complex geometries not aligned with mesh lines/surfaces. It also allows for easier development of an integrated model through coupling with already available finite volume-based multi-phase incompressible and compressible Navier–Stokes solvers in the same framework. The model itself was found to accurately simulate wave generation, propagation, and interaction with structures. However, this model also explicitly required artificial dissipation by way of a fourth-order damping correction scheme—a lower order scheme. Given the reasons discussed previous, this is not desirable, and it would be beneficial if the model did not have to use it. Indeed, no test cases were done over a large scale to examine if the model suffered from the sort of energy loss that is known to occur when using this type of technique. For this reason, there is a degree of uncertainty as to whether the model is applicable to large-scale and long-time simulations.

Our aim is to develop a new method that can stabilise the computation of FNPF models without using any of the aforementioned undesirable techniques that involve artificial damping. The new method should be physically sound, accurate, and robust for wave hydrodynamics. At the same time, it should be simple and easy to implement, economic for use, and incur no significant extra computational cost. In the present work, we propose using a more natural and mathematically sound numerical scheme to resolve the instability issue for FNPF models—consequently avoiding the use of any technique that involves significant artificial dissipation. To assess the effectiveness of the proposed method, we implement it in the finite volume-based FNPF model of Lin et al. (2021). The new model is systematically examined through a series of test cases including the propagation, focusing, and shoaling of nonlinear waves. In addition, comprehensive comparisons are made to evaluate the performance of the new model in terms of energy conservation.
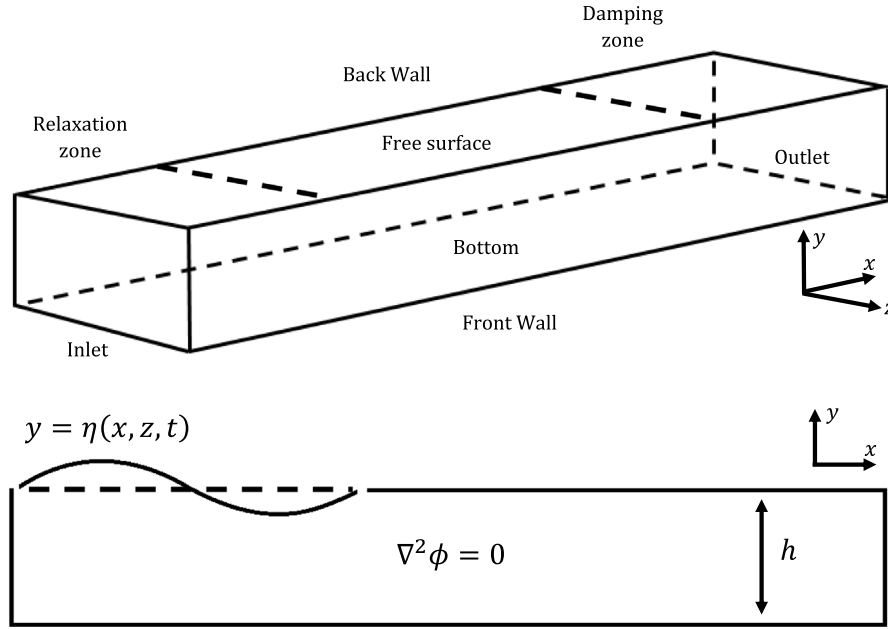
Fig. 1. Sketch of the three-dimensional numerical wave tank.

The remainder of this paper is laid out as followed. First, we give an overview of the mathematical formulation and numerical implementation of the Lin et al. (2021) model. Next, we give our methodology: reasons as to why the instability may be occurring and how to solve it, as well as the new computational formulation arising from this. Then, a number of test cases are presented, with numerical solutions from the new model validated against existing numerical, experimental, and analytical solutions. Lastly, we draw conclusions from our work and set out plans for further work.

2. Mathematical formulation and numerical implementation

Under potential flow theory, we assume that the flow is incompressible, inviscid, and irrotational. In the computational domain, a Cartesian coordinate system is defined with the y-axis pointing vertically upwards, and with the still free-surface water level defined as the xz-plane—as shown in Fig. 1. Furthermore, the free-surface elevation from the still water level is defined as the function $\eta(x, z, t)$ where t is the time. The governing equation in the fluid domain is Laplace's equation

$$\nabla^2 \phi = 0, \tag{1}$$

where $\phi(x, y, z, t)$ is the velocity potential. The nonlinear kinematic and dynamic boundary conditions (KBC and DBC respectively) – both satisfied at the free surface – are given as

$$\frac{\partial \eta}{\partial t} = \frac{\partial \phi}{\partial y} - \frac{\partial \phi}{\partial x}\frac{\partial \eta}{\partial x} - \frac{\partial \phi}{\partial z}\frac{\partial \eta}{\partial z} \quad \text{at} \quad y = \eta(x, z, t), \tag{2}$$

$$\frac{\partial \phi}{\partial t} = -g\eta - \frac{1}{2}\nabla\phi \cdot \nabla\phi \quad \text{at} \quad y = \eta(x, z, t), \tag{3}$$

where g is the gravitational acceleration.

As mentioned in the introduction, the majority of FNPF models adopt the MEL approach first outlined by Longuet-Higgins and Cokelet (1976). To understand why, consider the free-surface boundary conditions (2)–(3) which are given in the Eulerian description. For the simulation of water-wave problems, they clearly need to be satisfied on a moving boundary surface, in which case a Lagrangian description must be used. Hence, in the MEL approach, the Laplace problem is solved in the fluid domain from an Eulerian point of view, whilst the moving free-surface boundary is updated from a Lagrangian point of view.

Thus, when a free-surface node is moving with velocity **v**, the free-surface boundary conditions (2)–(3) can be modified by considering the material derivative

$$\frac{\delta()}{\delta t} = \frac{\partial()}{\partial t} + \mathbf{v} \cdot \nabla().$$

In a full-Lagrangian approach, free-surface nodes move with the motion of water particles, i.e., $\mathbf{v} = \nabla\phi$. However, this approach requires the free-surface nodes to be rearranged at every time step to prevent them from piling up. In contrast, in a semi-Lagrangian approach, free-surface nodes move only with the vertical motion of water particles, i.e., $\mathbf{v} = (0, \frac{\delta\eta}{\delta t}, 0)$. In this case, rearrangement of the free-surface nodes is unnecessary, making the method much simpler. This semi-Lagrangian approach is the one adopted by Lin et al. (2021) and in this work, meaning that the free-surface boundary conditions can be rewritten as

$$\frac{\delta\eta}{\delta t} = \frac{\partial\phi}{\partial y} - \frac{\partial\phi}{\partial x}\frac{\partial\eta}{\partial x} - \frac{\partial\phi}{\partial z}\frac{\partial\eta}{\partial z} \quad \text{at} \quad y = \eta(x, z, t), \tag{4}$$

$$\frac{\delta\phi}{\delta t} = -g\eta - \frac{1}{2}\nabla\phi \cdot \nabla\phi + \frac{\delta\eta}{\delta t}\frac{\partial\phi}{\partial y} \quad \text{at} \quad y = \eta(x, z, t). \tag{5}$$

Lin et al. (2021) then use a different but equivalent form of the KBC, presented in terms of the fluid particle velocity $\mathbf{U}_\eta$ at the free surface and the unit normal vector **n** of the free surface, as shown by Mayer et al. (1998). This leads to the KBC being rewritten as

$$\frac{\delta\eta}{\delta t} = \frac{\mathbf{U}_\eta \cdot \mathbf{n}}{n_y}, \tag{6}$$

where n_y is the vertical component of **n**.

To complete the boundary value problem in the NWT, additional conditions are required at the remaining boundaries. For problems involving wave generation, a relaxation zone is placed near the inlet boundary of the computational domain, as shown in Fig. 1. Conversely, a damping zone is placed near the outlet boundary for wave absorption. The mathematical details of each can be found in Lin et al. (2021) but are omitted here. Moreover, the front, back, and bottom are treated as fixed solid boundaries, meaning the impermeable boundary condition is used at each

$$\frac{\partial\phi}{\partial\mathbf{n}} = 0. \tag{7}$$

As mentioned in the introduction, the Lin et al. (2021) model was developed within the framework of OpenFOAM which implements

a cell-centred, co-located Finite Volume Method (FVM) on a three-dimensional structured or unstructured polyhedral mesh. Full details of the numerical implementation in OpenFOAM are found in Lin et al. (2021), here we only highlight that the computational mesh is updated at every time step to account for the motion of the free surface, with the mesh moving only in the vertical y-direction according to the semi-Lagrangian approach—as previously detailed. Furthermore, as mentioned in the introduction, Lin et al. (2021) employ a fourth-order damping correction scheme to ensure stability. For a quad cell of the free surface mesh, two nodes on the opposite corner are not direct but indirect donors to each other in the calculation of artificial dissipation. Full details of this scheme can be found in Lin et al. (2021), but here we note that the key parameters that control the amount of dissipation are the 'correction coefficient' β_{FODC}, shown in equation (16) of Lin et al. (2021), and the damping frequency (in time steps). We refer to these parameters throughout this paper.

3. Methodology

3.1. Hypothesis

As mentioned previously, the direct source of the sawtooth instability in FNPF models has never been definitively proven. However, it is clear that there is an accumulation of numerical error in the model; also, given that the free surface is where the sawtooth manifests, it is reasonable to assume that this error arises when updating the free-surface boundary conditions (Longuet-Higgins and Cokelet, 1976). In addition, it is well known that the numerical solution procedure for problems governed by Laplace's equation with Dirichlet and/or Neumann boundary conditions generally provides smooth results, but in the case of FNPF models, the free-surface boundary conditions are nonlinear and coupled, and this instead poses significant difficulties. Given this, we hypothesise that the use of a numerical scheme which does not properly take into account the physical characteristics of these boundary condition equations – particularly the KBC equation – is a major cause of error and instability.

To expand on this hypothesis, let us consider the characteristics of the KBC (4). Clearly, this equation is very similar to the 2-D advection equation but instead has a source term $F(y) = \frac{\partial \phi}{\partial y}$. Furthermore, given that the free-surface equations are a coupled set of equations, the evolution of the free-surface elevation η over time is dependent on the evolution of the velocity potential ϕ. As a consequence, the KBC is not hyperbolic like the advection equation, but is very similar so can instead be considered as advection dominated. It is well known that these sorts of equations are notoriously difficult to handle by using classical numerical schemes; hence, we instead propose using a different method to discretise the advection terms in the KBC in the Lin et al. (2021) model.

In order to match the order of numerical solution accuracy of the governing equation (1), the new method for the KBC equation should be at least second order. The new method should also be physically sound, accurate, and robust for wave hydrodynamics. At the same time, it should not be over complicated, but simple and easy to implement, and economic for use. Considering these requirements, we propose a second-order scheme motivated by a total variation diminishing (TVD) approach. TVD schemes are a class of *high-resolution schemes* for hyperbolic partial differential equations that are known to produce solutions free from spurious oscillations whilst remaining accurate around shocks and discontinuities. In particular, they are proven to produce oscillation-free solutions when used to discretise advection terms in advection-dominated equations like the KBC. In view of this, we will investigate whether such a method can effectively discretise the advection terms in the KBC, and consequently successfully stabilise the FNPF model.

A key advantage of TVD schemes is that they can also aptly handle sharp gradients which is of particular importance when it comes to

modelling steep waves. In this situation, the proposed TVD method is the perfect fix due to its monotonicity-preserving property. This is whereby, in the face of a sharp gradient, the numerical solution remains monotone before and after the advection terms are calculated, ensuring that there are no new local extrema—which is exactly what occurs in the formation of a sawtooth. The key to ensuring the scheme is monotonicity preserving is the flux limiter which directly modifies the advective fluxes in the scheme so that the total variation of the solution does not increase in time. Furthermore, as already outlined, the TVD method is robust and computationally efficient, as well as retaining second-order solution accuracy. Finally, the TVD method is simple and suited to a wide range of applications—no tuning of parameters is required. This is in contrast to a number of FNPF models (such as Lin et al. (2021)) in which the amount of artificial dissipation needs to be tuned for different cases in order to ensure stability. Note that, to the knowledge of the authors, such an attempt to implement such a method in FNPF models has not been reported in the literature.

3.2. Computational formulation

Time integration in the Lin et al. (2021) model was carried out using the first-order Euler scheme; we do the same in the present work. Moreover, for simplicity, we only consider a two-dimensional NWT in this formulation. However, the extension to three dimensions is straightforward by following the same logic. The computational mesh in OpenFOAM is three dimensional, but it can still be used for two-dimensional models by using a single cell in the z-direction. Clearly this works because the FVM is cell centred, so all information is stored in the same two-dimensional xy-plane. Furthermore, in this work, we only consider a structured computational mesh due to the fact we only use this FNPF model for wave propagation and wave–wave interaction. Finally, as already mentioned, we construct the method for the advection terms by closely following the TVD methodology.

We start by writing the KBC in 2-D form as

$$\frac{\delta \eta}{\delta t} = v - u\frac{\partial \eta}{\partial x}, \quad \text{where } v = \frac{\partial \phi}{\partial y} \text{ and } u = \frac{\partial \phi}{\partial x}. \tag{8}$$

Now, let $i - \frac{1}{2}$ and $i + \frac{1}{2}$ denote the left and right edge respectively of a computational free-surface mesh cell i. Then, using the Euler method for time integration, the update for η in cell i can be written as

$$\eta_i^{n+1} = \eta_i^n + v_i^n \Delta t - \frac{u_i^n \Delta t}{\Delta x}(\eta_{i+\frac{1}{2}}^n - \eta_{i-\frac{1}{2}}^n). \tag{9}$$

If $u_i \geq 0$, setting $\eta_{i+\frac{1}{2}} = \eta_i$ and $\eta_{i-\frac{1}{2}} = \eta_{i-1}$ recovers the First Order upwind (FOU) scheme—a first-order TVD scheme that is known to be the most numerically stable but suffers severely from numerical dissipation. For a second-order evaluation of $\eta_{i+\frac{1}{2}}$ and $\eta_{i-\frac{1}{2}}$, a correction term needs to be added. This is where the idea of a flux limiter and the TVD property comes in.

3.2.1. TVD property

To construct a TVD scheme for the advection terms, we first need to define what actually makes a scheme TVD. Firstly, consider that an explicit numerical scheme used to calculate some variable f in cell x_i, and at time t_{n+1} generally has the form

$$f_i^{n+1} = G(f)_i^n = G(f_{i-p}^n, \ldots, f_i^n, \ldots, f_{i+q}^n), \quad p = 1, 2, \ldots, q = 1, 2, \ldots, \tag{10}$$

and is said to be *monotone* if and only if the function G is an increasing (or decreasing) function of all its arguments, i.e., G is monotonically increasing if

$$\forall f_i, f_j \text{ such that } f_i \leq f_j, \text{ we have } G(f_i) \leq G(f_j) \quad \text{(and vice versa).} \tag{11}$$

The scheme is then also said to be *monotonicity preserving* if

$$f_{i+1}^n \geq f_i^n \quad \forall i \implies f_{i+1}^{n+1} \geq f_i^{n+1} \quad \forall i. \tag{12}$$

A monotonicity-preserving scheme creates no new undershoots or overshoots in the solution, meaning that it should be free of spurious oscillations, and hence this is the type of scheme we want. To construct this sort of scheme, we first define the total variation of a data set $\{f_1, f_2, \ldots, f_{n-1}, f_n\}$, which is given as

$$TV(f) = \sum_{i=1}^{n-1} |f_{i+1} - f_i|. \tag{13}$$

The scheme is then said to be *total variation diminishing (TVD)* if

$$TV(f^{n+1}) \leq TV(f^n), \tag{14}$$

which will clearly be monotonicity preserving. Furthermore, it can be shown that a monotone scheme is TVD, and hence monotonicity preserving, so to construct a TVD scheme it is sufficient for the scheme to be monotone. For more details, please refer to the work of Harten (1983).

3.2.2. Flux limiter

Referring back to the update for η (9), it is clear that the second-order correction must ensure that the scheme for the advection terms is monotone, and hence TVD. The way we do this is by using a flux limiter. First we consider the generalised second-order upwind-biased evaluation of $\eta_{i+\frac{1}{2}}$ when $u_i \geq 0$,

$$\eta_{i+\frac{1}{2}} = \eta_i + \frac{1}{2}\psi(r_{i+\frac{1}{2}})(\eta_{i+1} - \eta_i). \tag{15}$$

Here, ψ is called the *flux limiter function*, dependent on r which is the ratio of upwind to downwind gradients of η for cell i. For example, given that $u_i \geq 0$ in (9) and (15), the ratio of upwind to downwind gradients is

$$r_{i+\frac{1}{2}} = \frac{\eta_i - \eta_{i-1}}{\eta_{i+1} - \eta_i}. \tag{16}$$

For the scheme to then be monotone and therefore TVD, as well as second order, the flux limiter function $\psi(r)$ must satisfy certain constraints derived by Sweby (1984) that are outlined in Appendix but are omitted here.

For the choice of flux limiter in the present work, we choose the Van Albada 2 limiter defined as

$$\psi(r) = \begin{cases} \dfrac{2r}{r^2+1}, & r > 0 \\ 0, & r \leq 0. \end{cases} \tag{17}$$

Incidentally, this limiter is actually only first-order accurate for $r > 1$. However, it still successfully produced sufficiently accurate results in the present work. In our future work, it would be interesting to assess the performance of other available flux limiters, but in the present work, the Van Albada 2 limiter can produce satisfactory solutions.

3.2.3. Final formulation

In addition to (15) and (16) at the right edge $i + \frac{1}{2}$, at the left edge $i - \frac{1}{2}$ we have

$$\eta_{i-\frac{1}{2}} = \eta_{i-1} + \frac{1}{2}\psi(r_{i-\frac{1}{2}})(\eta_i - \eta_{i-1}), \tag{18}$$

where

$$r_{i-\frac{1}{2}} = \frac{\eta_{i-1} - \eta_{i-2}}{\eta_i - \eta_{i-1}}. \tag{19}$$

Finally, using (15), (16), (17), (18), and (19) in (9) gives the update for η in cell i given that $u_i \geq 0$

$$\eta_i^{n+1} = \eta_i^n + v_i^n \Delta t - \frac{u_i^n \Delta t}{\Delta x}\left\{[\eta_i^n + \frac{1}{2}\psi(r_{i+\frac{1}{2}})(\eta_{i+1}^n - \eta_i^n)] \right.$$
$$\left. - [\eta_{i-1}^n + \frac{1}{2}\psi(r_{i-\frac{1}{2}})(\eta_i^n - \eta_{i-1}^n)]\right\}, \tag{20}$$

where $\psi(r_{i+\frac{1}{2}})$ and $\psi(r_{i+\frac{1}{2}})$ are calculated accordingly. Note that an equivalent result can be derived in the same way for when $u_i < 0$ but is omitted here. Please also note that we refer to the new improved model as the 'stabilised model' throughout.

4. Validation and discussion

To comprehensively validate the proposed method, we consider three well-known test cases. The first test case is regular wave propagation in a three-dimensional numerical wave tank, split into two separate cases in terms of the type of wave generated, with results compared to analytical solutions and those of Lin et al. (2021). The second test case is focused wave propagation in which we simulate irregular extreme wave events. For this test case we follow and compare our results to the numerical and practical experiments of Ning et al. (2009). For the third test case we consider 2-D and 3-D wave shoaling to capture the transformation of propagating waves due to variable bathymetry. In 2D, we follow the experiments of Beji and Battjes (1993, 1994), whereas in 3D we follow the experiments of Whalin (1971). Finally, we prove the superiority of the stabilised model over the Lin et al. (2021) model in terms of energy conservation. It should be noted that, for each case, the first thing we establish is whether we have eliminated the sawtooth instability without using numerical damping. Only then do we consider the accuracy of our results. In addition, as already stated, numerical damping is required for each validation test case when it comes to the Lin et al. (2021) model, and hence any Lin et al. (2021) results used for comparison in this section are when damping is being used—unless of course stated otherwise.

During each simulation, the time step Δt is automatically calculated using an adaptive procedure based on the Courant–Friedrichs–Lewy (CFL) condition (21), where C is the Courant number, Δx the local cell width, and $C_{\max}$ the maximum Courant number which is fixed at the start of the simulation.

$$C = \frac{u \Delta t}{\Delta x} \leq C_{\max}. \tag{21}$$

For most cases in the present work, unless stated otherwise, a value of $C_{\max} = 0.2$ is used. This ensures that the time step is small enough for a convergent and accurate solution.

4.1. Regular wave propagation

In this first validation test case, we simulate regular wave propagation in a 3-D NWT. As illustrated in Fig. 1, a relaxation and damping zone are introduced into the tank in order to generate and absorb progressive waves respectively. Two particular types of target wave – second-order Stokes and fifth-order Stokes – are considered separately.

4.1.1. Second-order Stokes waves

The geometric setup here is the same as Lin et al. (2021) with the NWT having length 12.6 metres (m) in the x-direction, width 1.0 m in the z-direction, and depth 0.505 m in the y-direction. Second-order Stokes waves are generated in the relaxation zone according to the set of input wave parameters listed in Table 1. In addition, the relaxation and damping zones are both chosen to be one wavelength long (3.164 m), with the tank in total being approximately four wavelengths long.

In order to test performance, we first carry out a mesh-sensitivity study. Four different mesh configurations are chosen and are each listed in Table 2, with an example mesh shown in Fig. 2. We can also see from this that the mesh is refined in the y-direction near the free surface in order to increase resolution. It is done in a way such that the cell at the top has vertical width $1/10$ of the cell at the bottom. In order to then actually measure free-surface elevation, wave gauges are positioned at $x = 0.05$ m (WG1) and $x = 6.3$ m (WG2). Here, the results recorded at WG2 are essentially a measure on the ability of the model to reproduce the analytical second-order Stokes waves generated in the
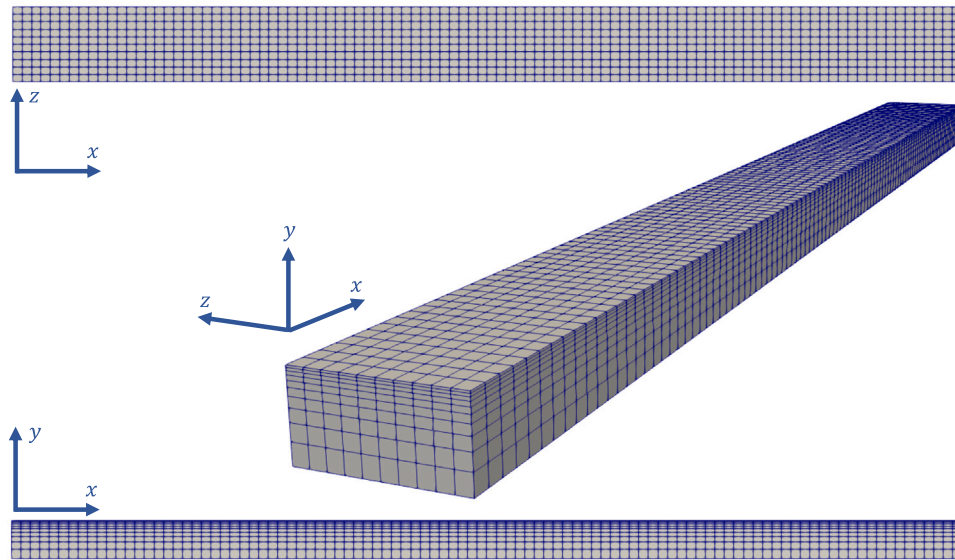
Fig. 2. Illustration of mesh configuration M3 for the second-order Stokes case.

Table 1
Wave parameters for second-order Stokes wave.

Wave	Amplitude: A (m)	Height: H (m)	Period: T (s)	Wavelength: λ (m)	Water depth: h (m)
Stokes 2nd	0.06	0.12	1.63	3.164	0.505

Table 2
Mesh configurations for sensitivity study: second-order Stokes case.

Mesh	Configuration $x \times y \times z$	Cells per wavelength	Lin et al. (2021) crash time (s)
M1	$60 \times 10 \times 10$	15	11.15
M2	$80 \times 10 \times 10$	20	10.65
M3	$100 \times 10 \times 10$	25	9.75
M4	$120 \times 10 \times 10$	30	9.55

relaxation zone at WG1, and hence how we test performance. Finally, the simulation time is 40 s.

Before we discuss the results from the stabilised model, we first want to illustrate the problem of the sawtooth instability. To do this, we ran a preliminary analysis under the same conditions outlined above using the Lin et al. (2021) model—but with NO numerical damping applied. What we found was that, for each mesh configuration, the simulation crashes before the completion time, as listed in Table 2. Fig. 3 then shows the free surface profile at the crash time for configuration M3. The sawtooth-like free-surface profile can clearly be seen at the left most peak and second to left most trough. This sort of sawtooth-like wave profile actually becomes faintly visible almost immediately after the simulation starts, but slowly becomes more defined as each wave propagates down the tank.

Now, for the stabilised model, Fig. 5(a)–(c) show the time histories of the free-surface elevation at WG2 for the different mesh configurations listed in Table 2, plotted with the second-order Stokes solution produced at WG1. Firstly, the key thing to note is that the simulation is stable, does not crash, and the free surface does not develop a sawtooth profile—all without using numerical damping or smoothing. The solution is also clearly converging to the analytical, agreeing with the recommendation made by Lin et al. (2021) that having more than 25 cells per wavelength is required to ensure a good level of stability and accuracy in the NWT.

For this case, it also seems that a smaller value of C_{max} is necessary to produce convergent solutions. The results in Fig. 5(a)–(c) were actually produced using a value of $C_{max} = 0.01$, a value that we determined by investigating temporal convergence using mesh configuration M3. Fig. 4(a)-(c) show the time histories of the free-surface elevation at WG2 for different values of C_{max}, plotted with the second-order Stokes solution produced at WG1. What we find is that a value of at most 0.01 is required for sufficient accuracy. This is an anomaly in the present work as all other test cases converged for the set value $C_{max} = 0.2$ stated previous. A potential reason for this is the simplicity of the case itself: only a coarse mesh is required for convergence. The other cases in this paper are much more complex and require finer mesh resolutions as a result, meaning that Δx in (21) is smaller and hence C_{max} can be larger (whilst also being mindful of u also).

4.1.2. Fifth-order Stokes waves

We now generate fifth-order Stokes waves in the relaxation zone rather than second-order Stokes waves; the input wave parameters are listed in Table 3. The nonlinearity of these waves is stronger so we should thoroughly test the performance capabilities of the stabilised model, both with regards to stability and accuracy. Again the same setup is used as Lin et al. (2021): the NWT has dimensions 100 m × 0.7 m × 1.0 m in the x, y, and z directions respectively. However, we now choose a single mesh configuration of $1080 \times 30 \times 5$, corresponding to 50 cells per wavelength. Note this is clearly much higher than the second-order Stokes case owing to the stronger nonlinearity of the input waves. Again, the mesh is refined in the y-direction such that the cell at the top has vertical width 1/10 of the cell at the bottom. Finally, the simulation time is again 40 s.

Fig. 6 then shows the time histories of the free-surface elevation for the stabilised model, Lin et al. (2021) model, and analytical fifth-order Stokes solution at various gauges in the NWT. Again, the key thing to note is that the simulation is stable with no sawtooth instability—all without using numerical damping or smoothing. This provides clear
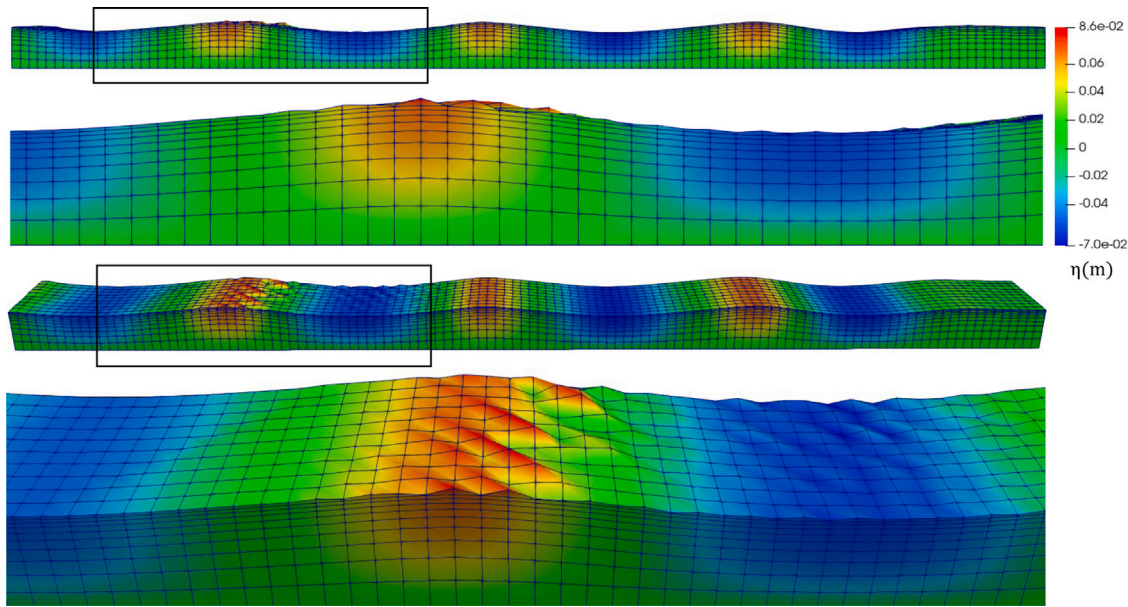
Fig. 3. Snapshot of the free-surface at the crash time for configuration M3.
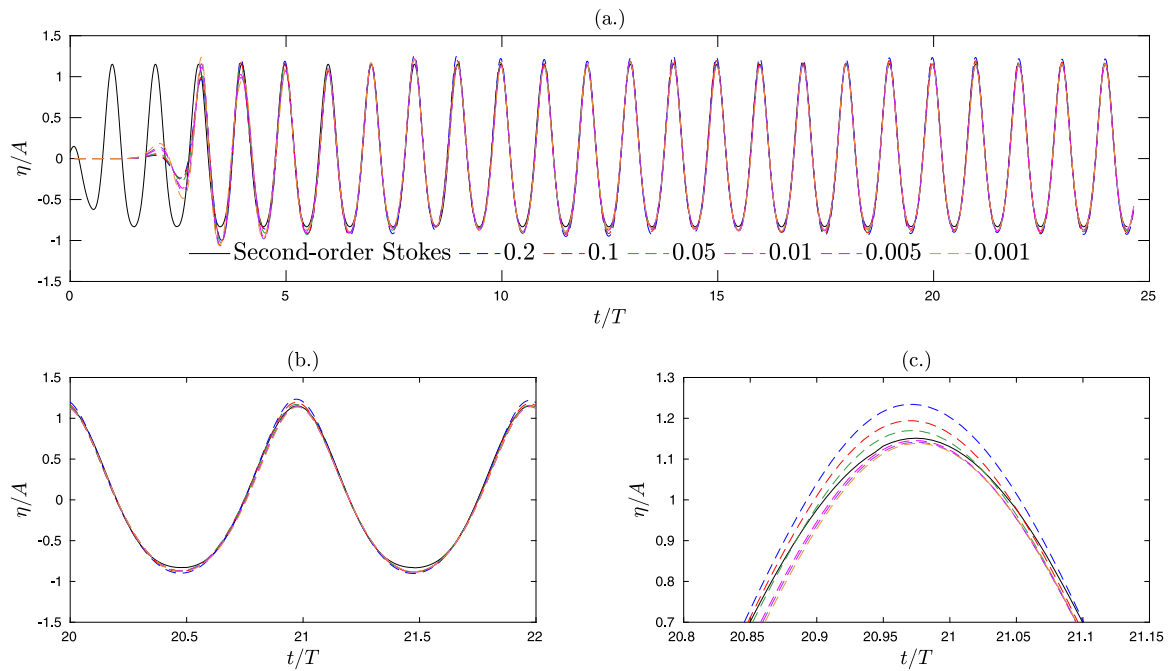

Fig. 4. Time histories of free-surface elevation at WG2 for different values of $C_{\max}$ and analytical second-order Stokes solution: (a.) Whole simulation, (b.) $t/T \in [20, 22]$, (c.) $t/T \times \eta/A \in [20.8, 21.15] \times [0.7, 1.2]$.

Table 3
Wave parameters for fifth-order Stokes wave.

Wave	Amplitude: A (m)	Height: H (m)	Period: T (s)	Wavelength: λ (m)	Water depth: h (m)
Stokes 5th	0.125	0.25	2	4.62	0.7

evidence that the stabilised model has the capacity to remain stable in the face on nonlinear waves. In addition, the solution is clearly also very accurate, even for the wave gauge furthest down the tank. A similar level of accuracy is also displayed when compared to the Lin et al. (2021) model for which a value $\beta_{FODC} = 0.05$ with a frequency of 5 time steps is used to ensure stability.

4.2. Focused wave propagation

In addition to the propagation of regular waves, we can also consider the propagation of irregular waves. Of particular importance to wave–structure models is the existence of extreme waves. An irregular sea state in any given region is random, consisting of many different
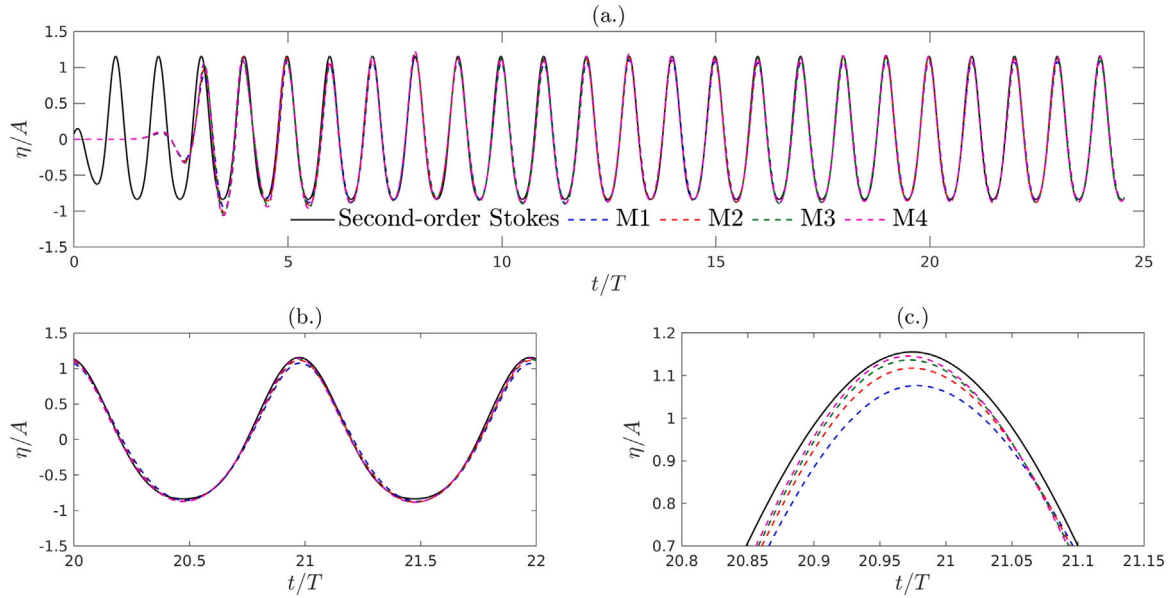
Fig. 5. Time histories of free-surface elevation at WG2 for different mesh configurations and analytical second-order Stokes solution: (a) Whole simulation, (b) $t/T \in [20, 22]$, (c) $t/T \times \eta/A \in [20.8, 21.15] \times [0.7, 1.2]$.

incident waves. The nonlinear interactions between these waves can result in ones that are much larger than what would be expected: these are called extreme waves. In order to replicate these extreme wave events in a numerical wave tank, the most widely utilised method is to use NewWave theory to generate focused waves. When using NewWave theory, a group of localised regular waves are derived from a measured or theoretical waves spectrum such as JONSWAP or Pierson–Moskowitz. These individual wave components are then superposed so that they constructively interfere to build up a larger irregular wave. In addition, the phase of each wave component is adjusted so that they each focus simultaneously at a specific time and location. The result is a *focused* extreme wave representative of the underlying spectrum.

For this test case, we again use a relaxation zone for wave generation and a damping zone for absorption. As mentioned above, focused wave generation is realised through the linear superposition of a finite number of regular wave components. Hence, the first-order free-surface wave elevation using N components is defined as

$$\eta^{(1)} = \sum_{i=1}^{N} A_i \cos\theta_i, \tag{22}$$

where A_i is the amplitude of each component and θ_i is the phase of each component. Moreover, the phase is defined as

$$\theta_i = k_i x - \omega_i t - \epsilon_i, \tag{23}$$

where k_i is the wavenumber, and ω_i the angular frequency, of each component. As also previously mentioned, the phase of each component is adjusted so that the waves focuses at a specific time and location. To do this, ϵ_i in (23) is defined as

$$\epsilon_i = k_i x_0 - \omega_i t_0, \tag{24}$$

where t_0 is called the *focus time* and x_0 is called the *focus location*. Consequently, similarly to the free-surface elevation $\eta^{(1)}$, the first-order velocity potential is defined as

$$\phi^{(1)} = \sum_{i=1}^{N} \frac{g A_i}{\omega_i} \frac{\cosh(k_i[y+h])}{\cosh(k_i h)} \sin(k_i(x-x_0) - \omega_i(t-t_0)). \tag{25}$$

In addition, linear superposition also gives the amplitude A_i, for each wave component i, as

$$A_i = A_I \frac{S_i(f)\Delta f}{\sum_{i=1}^{N} S_i(f)\Delta f}, \tag{26}$$

where A_I is the input amplitude of the focused wave, $S_i(f)$ is the spectral density, and Δf is the increment frequency. In this paper, $S_i(f)$ refers to the JONSWAP spectrum:

$$S_i(f) = \frac{5}{16} H_s^2 f_p^4 f_i^{-5} \exp\left(-\frac{5}{4}\left(\frac{f_p}{f_i}\right)^4\right) \gamma^{\exp\left(\frac{-(f_i - f_p)^2}{2\sigma^2 f_p^2}\right)}, \tag{27}$$

where H_s is the significant wave height, $\gamma = 3.3$ is the peak-enhancement factor, f_p is the peak spectral frequency, and σ is the spectral width parameter defined as

$$\sigma = \begin{cases} 0.07 & \text{for } f_i \leq f_p, \\ 0.09 & \text{for } f_i > f_p. \end{cases} \tag{28}$$

We see from the spectrum (27) that, in order to generate each wave component, we need to input H_s (which is just A_I) and f_p, as well as set a frequency bandwidth $f \in [f_{\min}, f_{\max}]$. In addition, given that we then know the bandwidth $[f_{\min}, f_{\max}]$ and number of components N, we can also calculate the frequency Δf in (26).

In this paper, we also add the second-order free-surface elevation and velocity potential so that

$$\eta = \eta^{(1)} + \eta^{(2)}, \tag{29}$$

$$\phi = \phi^{(1)} + \phi^{(2)}. \tag{30}$$

Details of the formulation for $\eta^{(2)}$ and $\phi^{(2)}$ can be found in papers by Ning et al. (2008, 2009), but are omitted here.

For the test case itself, we follow the physical and numerical experiments carried out by Ning et al. (2009). For the physical experiments, a wave tank with dimensions 69.0 m × 0.5 m × 3.0 m was used. In the experiments, four extreme wave cases – based on NewWave theory – were investigated with different input amplitudes. In this paper, we validate the stabilised model using cases 1 and 3 in particular; the corresponding input wave characteristics are listed in Table 4. Note that T_p and λ_p are the period and wavelength for the characteristic wave for that particular group, which is taken as the wave corresponding to the peak amplitude (for that group).

In the numerical experiments by Ning et al. (2009), the 3-D NWT has dimensions $5\lambda_p$ m × 0.5 m × $\lambda_p/10$ m. However, using a 3-D tank seems unnecessary as there is no variation in the z–direction; in addition, the width λ_p is very small. Consequently, in this paper, we use a 2-D NWT with dimensions $5\lambda_p$ m × 0.5 m to improve efficiency
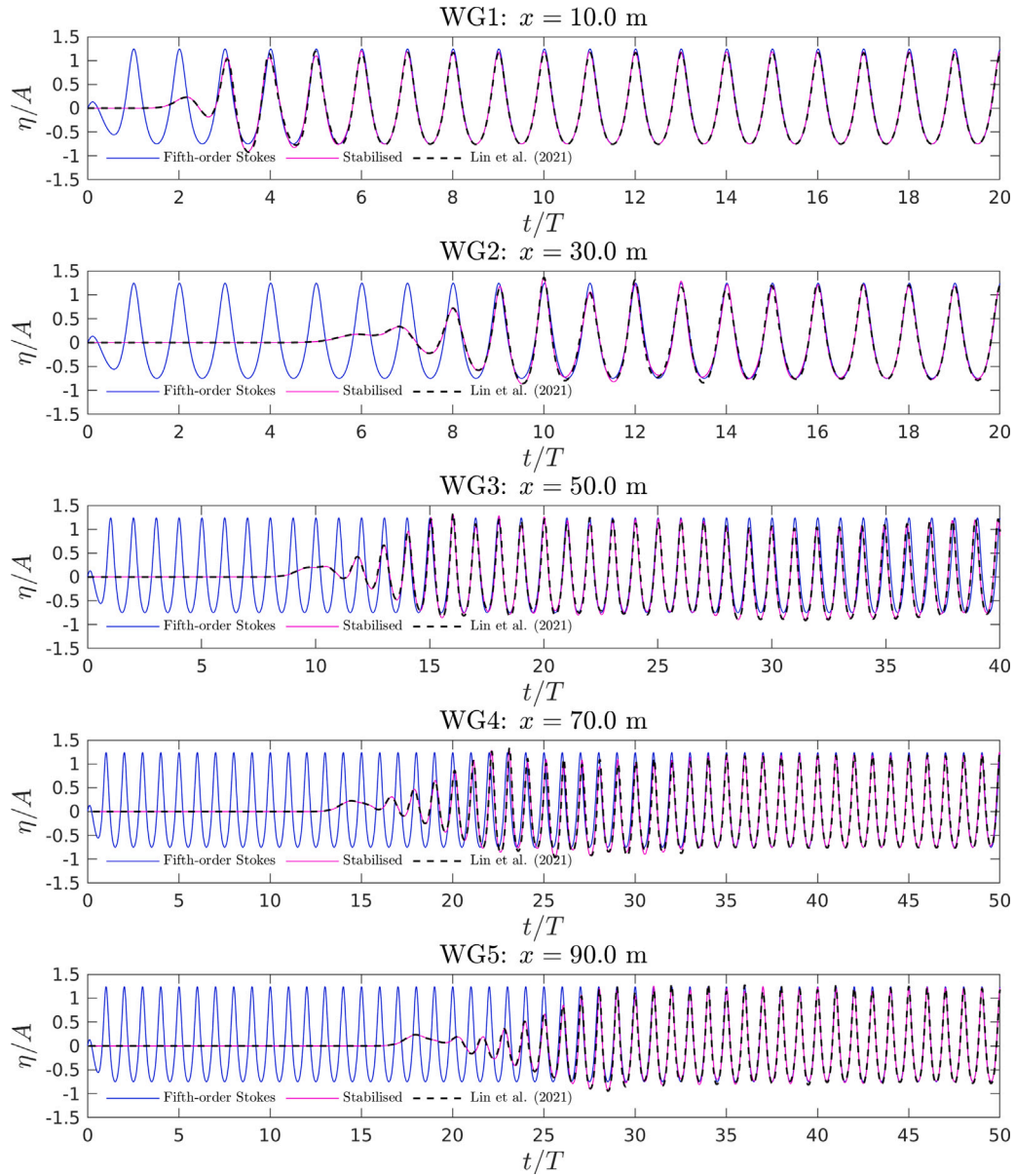
Fig. 6. Time histories of free-surface elevation for the stabilised model, Lin et al. (2021) model, and analytical fifth-order Stokes solution at various wave gauges in the NWT. Please note that the upper limits of the time intervals in these panels are not the same.

Table 4
Input wave characteristics for cases NING1 and NING3.

Case	Frequency band (Hz)	Peak frequency: f_p (Hz)	Period: T_p (s)	Input amplitude: A_I (m)	Wavelength: λ_p (m)
NING1	$f \in [0.6, 1.2]$	0.83	1.2	0.0313	2
NING3	$f \in [0.6, 1.4]$	0.8	1.25	0.0875	2.18

with a negligible difference in results. Moreover, the relaxation and damping layer are the same length as Ning et al. (2009), i.e., λ_p and $2\lambda_p$ respectively. All these dimensions are more clearly listed for each case in Table 5. The corresponding focus location and time are also given by Ning et al. (2009) as $x_0 = 1.5\lambda_p$ and $t_0 = 8T_p$ respectively. These are more clearly listed for each case in Table 6. Finally, for case NING1 we use 31 wave components, whereas for case NING3 we use 41. The difference is owed to the increased steepness and nonlinearity of the focused wave in NING3.

To begin, we first undertook a mesh convergence study for case NING1 to assess accuracy and to determine the best mesh configuration for the steeper case NING3. Four different mesh configurations are
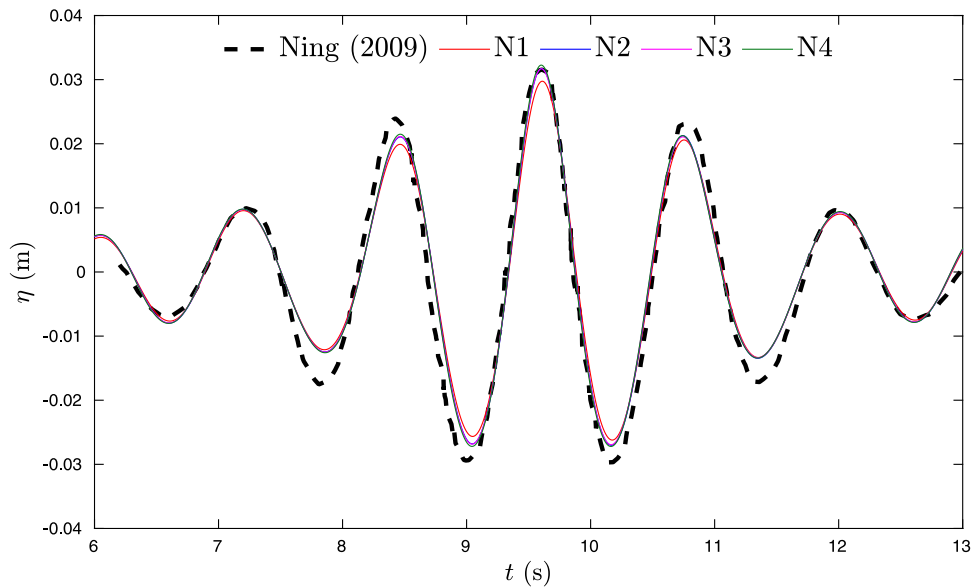
Table 5
Dimensions of NWT for cases NING1 and NING3.

Case	NWT dimensions $x \times y$ (m)	Relaxation zone	Damping zone
NING1	10×0.5	[0, 2]	[6, 10]
NING3	10.9×0.5	[0, 2.18]	[6.54, 10.9]

chosen and are listed in Table 7. Again, the mesh is refined in the y-direction such that the cell at the top has vertical width $1/10$ of the cell at the bottom. Fig. 7 then shows the time histories of free-surface elevation at the focus location x_0, plotted with the experimental solution from Ning et al. (2009). Again, the simulation is stable with

Table 6

Input and real focusing properties for cases NING1 and NING3.

Case	Input focus location: x_0 (m)	Input focus time: t_0 (s)	Actual focus location: x_1 (m)	Actual focus time: t_1 (s)
NING1	3	9.6	3	9.6
NING3	3.27	10	3.575	10.16

Fig. 7. Time histories of free-surface elevation at the input focus location x_0 for different mesh configurations and experimental solution from Ning et al. (2009).

Table 7

Mesh configurations for sensitivity study: case NING1.

Mesh	Configuration ($x \times y$)	Cells per wavelength
N1	75×10	15
N2	100×10	20
N3	125×10	25
N4	150×10	30

no sawtooth instability. In terms of convergence, the solution is clearly converging with there being minimal difference between the results for configurations N1, N2, N3, and N4—all of which are very accurate. Therefore, we choose the middle configuration N3 – corresponding to 25 cells per wavelength – for case NING3.

Moving on to NING3, we can see from Table 4 that the input amplitude A_I is almost three times larger than for case NING1. This also means that the focused wave will be steeper and be more strongly nonlinear. Consequently, we expect that the focusing time will be delayed and the focusing location will be shifted downstream. The is an effect reported not only by Ning et al. (2009), but also other authors such as Westphalen et al. (2012), Bihs et al. (2017), and Wang et al. (2019), with the cause in main being attributed to nonlinear wave–wave interaction as the wave group evolves—something that becomes more prominent with increased nonlinearity as we see with case NING3. Given this, we need to find the true focus time t_1 and location x_1. To do this we output the wave profile at close time intervals around the input focus time $t_0 = 10$, as done by Wang et al. (2019). By doing this we can then find the wave profile with the largest peak amplitude, its corresponding focusing location which will be x_1, and the corresponding time which will be t_1. By this method, t_1 is found to be 10.16 s and x_1 is found to be 3.575 m, both of which are also listed in Table 6. Fig. 8(a) then shows the wave profiles for both t_0 and t_1 where we can see that the central crest at t_1 is slightly higher than at t_0. Fig. 8(b) then also shows the time histories of free-surface elevation at both x_0 and x_1 where we can clearly see the delay in focal time due to increased nonlinearity. Finally, Fig. 8(c) compares

the time history of free-surface elevation at the real focal location x_1 with the experimental results from Ning et al. (2009), from which we can see a good agreement in results. Note that the delay in time and shift downstream is slightly smaller than the other works cited. It is reasonable to assume that this is due to the fact we use a relaxation zone to generate the focused wave in this work whereas the others use either a piston or paddle wavemaker.

What we can conclude then from this case is that the stabilised model can accurately replicate extreme wave events in a NWT without encountering the sawtooth instability. This is of particular importance when assessing the survivability of offshore structures: any structure must be able to survive the harshest conditions, no matter how rare they may be. Hence, when it comes to designing integrated models, we can be confident that this stabilised model can successfully act as the FNPF part when is comes to replicating these events.

4.3. Wave shoaling

In this section, two more complex test cases are considered to further validate the stabilised model—2-D and 3-D wave shoaling. Each case will establish how accurately the model can capture the transformation of propagating waves that occurs due to variable bathymetry. For the 2-D case, this is due to interaction with a submerged structure, whereas for the 3-D case, this is due to changing bottom topography.

4.3.1. 2-D shoaling

Starting with 2-D shoaling, we follow the experiments described by Beji and Battjes (1993, 1994) which investigated how interaction with a submerged trapezoidal bar affected wave propagation. The NWT in this case has dimensions 30 m × 0.4 m in the x and y directions respectively, but also has the aforementioned trapezoidal bar at the bottom boundary—as illustrated in Fig. 9. We use two sets of input wave parameters, B1 and B2, both listed in Table 8. B1 corresponds to the set used in Beji and Battjes (1994), whilst B2 corresponds to the set used in Beji and Battjes (1993). Note that the input waves B2 are approximately 4.6 times steeper than B1. Thus, the mesh configuration
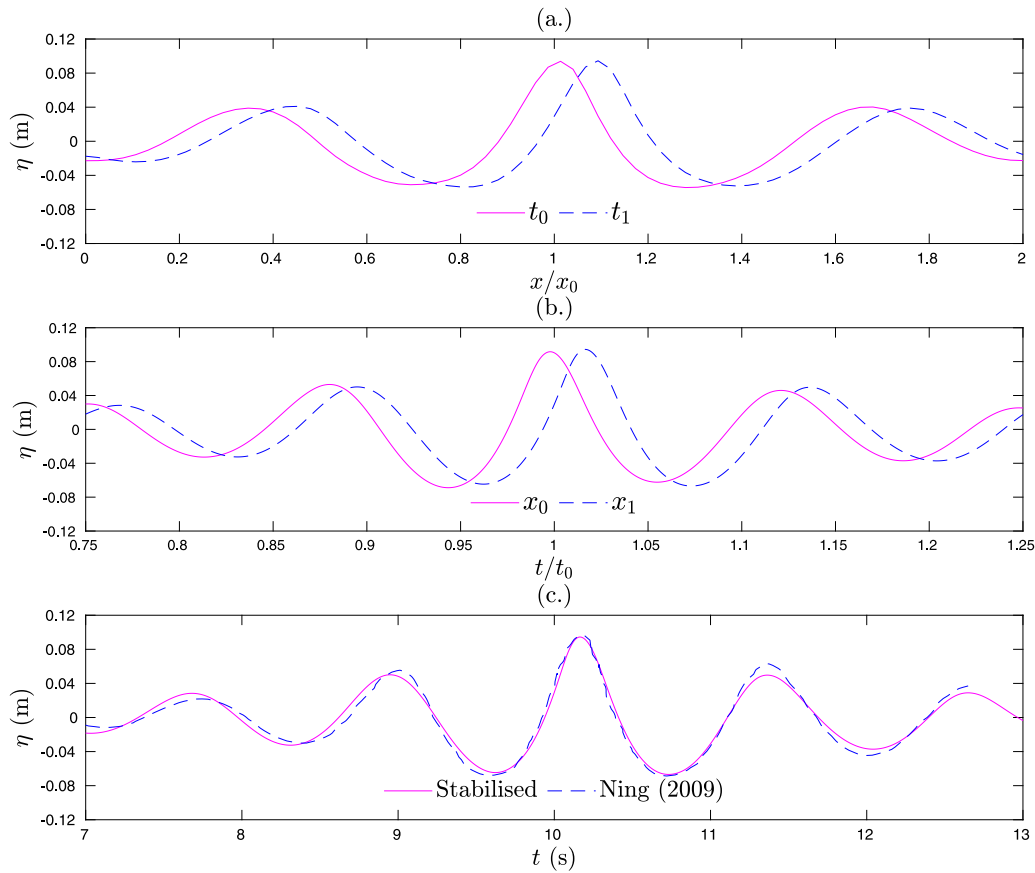
Fig. 8. (a.) Free-surface profile at input focus time t_0 and real focus time t_1. (b.) Time histories of free-surface elevation at input focus location x_0 and real focus location x_1. (c.) Time histories of free-surface elevation at real focus location x_1 and experimental solution from Ning et al. (2009).

Table 8
Wave parameters for 2-D and 3-D shoaling cases.

Case ID	Amplitude: A (m)	Height: H (m)	Period: T (s)	Wavelength: λ (m)	Water depth: h (m)	Steepness: H/λ
B1	0.01	0.02	2.02	3.737	0.4	0.005352
B2	0.018	0.036	1	1.4637	0.4	0.02460
W1	0.0195	0.039	1	1.4957	0.4572	0.02607
W2	0.0075	0.015	2	3.9095	0.4572	0.003837
W3	0.0106	0.0212	2	3.9095	0.4572	0.005423

Table 9
Mesh configurations for 2-D and 3-D shoaling cases.

Mesh	Configuration $x \times y \times z$
2D_M1	$1500 \times 20 \times 1$
2D_M2	$3000 \times 20 \times 1$
3D_M1	$1750 \times 30 \times 50$
3D_M2	$1750 \times 30 \times 100$

used for each is also different to account for the increased wave steepness and to ensure there is sufficient mesh resolution. For B1 we use configuration 2D_M1 listed in Table 9, whereas for B2 we use configuration 2D_M2. With both of these configurations, the mesh is not uniform. Instead, it is refined in the x-direction to increase resolution in the region $x \in [11, 21]$ where the wave shoaling phenomenon is significant. Furthermore, the mesh is again refined in the y-direction as was with the wave propagation test case. Note that in this case, comparisons are made with the Lin et al. (2021) model for which a value of $\beta_{FODC} = 0.2$ with a frequency of 1 time step is used to ensure stability.

Considering B1 first, Fig. 10 shows the time histories of the free-surface elevation for the stabilised model, Lin et al. (2021) model, and experimental solution of Beji and Battjes (1994) at various wave gauges in the NWT. Again, we must emphasise that the key point to acknowledge here is that no numerical damping is required to ensure stability for this case. In terms of accuracy, we see from Fig. 10 that the present results at WG1: $x = 2.0$ m are practically identical to the experimental solution and Lin et al. (2021) results, meaning that the target waves are produced well in the relaxation zone. Then from WG2: $x = 12.5$ m to WG8: $x = 21.0$ m we clearly observe the expected increase in amplitude and nonlinearity due to the presence of the submerged bar, with good agreements shown between the stabilised model and experimental solution. At WG's 5-8, the present results actually seem over predicted compared to the experimental data. However, this might be reasonable given that the more accurate potential flow simulation might over predict due to the absence of fluid viscosity.

Moving on to B2, Fig. 11 shows the analogous results but this time plotted with the experimental solution of Beji and Battjes (1993). Once again, the solution is stable and no numerical damping is required. In terms of accuracy, the results at WG1: $x = 6.0$ m – just before
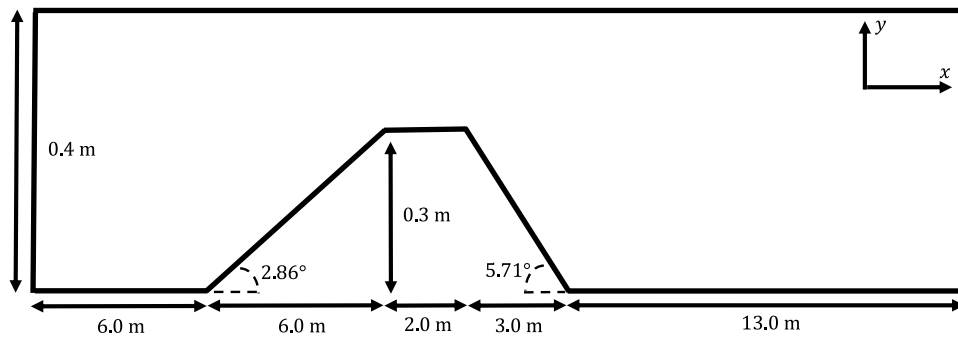
Fig. 9. Sketch of NWT for 2-D shoaling case (not to scale).

the submerged bar – agree well with the experimental solution and are identical to the Lin et al. (2021) results. Then from WG2: $x = 12.0$ m to WG4: $x = 14.0$ m – where the shoaling effects predominately occur – we clearly observe the expected increase in amplitude, with good agreements with the experimental solution and Lin et al. (2021) results. Lastly, at WG5: $x = 15.0$ m and WG6: $x = 16.0$ m, strong nonlinear effects can be observed and slight discrepancies between the stabilised model and experimental solution emerge. However, this is to be expected due to the high nonlinearity.

What we can conclude then from this case is that the stabilised model is able to accurately simulate the transformation of propagating waves that occurs due to interaction with a submerged structure, as well as capturing the ensuing highly nonlinear effects. Again, this is all without using numerical damping and without the appearance of the sawtooth instability.

4.3.2. 3-D shoaling

Now, for 3-D shoaling, we follow the experiments carried out by Whalin (1971). In this test case, the bottom topography is changing due to a submerged semi-circular slope. This will test the ability of the stabilised model to capture 3-D nonlinear effects associated with wave transformation rather than just 2D. The NWT in this test case has dimensions 35 m × 6.096 m in the x and z directions, but as mentioned, has varying water depth h which can be defined as the function

$$h(x,z) = \begin{cases} 0.4572, & 0 \leq x \leq 10.67 - G(z), \\ 0.4572 + \frac{1}{25}(10.67 - G(z) - x), & 10.67 - G(z) < x < 18.29 - G(z), \\ 0.1524, & 18.29 - G(z) \leq x \leq 35.0, \end{cases}$$

(31)

where $G(z) = \sqrt{z(6.096 - z)}$. The resulting semi-circular slope is illustrated visually in Fig. 12. For this case, three different sets of wave parameters are used: W1, W2, and W3—all listed in Table 8. For W2 and W3, we use mesh configuration 3-D_M1 listed in Table 9, whereas for W1 we use configuration 3-D_M2. This increased number of cells for W1 is down to the increased steepness and nonlinearity: W1 is approximately 6.8 times steeper than W2—the least steep. Again, as was with the 2-D shoaling case, the mesh is refined in the x and y directions to increase resolution in the shoaling area and free surface respectively.

The first thing to note from the results is that the simulation is stable for each of W1, W2, and W3. Fig. 13(a)–(c) then show the first three harmonic components – obtained by Fast Fourier Transform – along the streamwise central line of the NWT for the stabilised model, Shao and Faltinsen (2014), Engsig-Karup et al. (2009), and experimental results of Whalin (1971). Overall, for all three inputs, we see good agreements between the stabilised model results and those of the other cited works, even for the steepest input W1 (Fig. 13(a)). In addition, for W3, Fig. 14(a)–(d) show snapshots of the free surface at various times during the simulation. What we see in Fig. 14(a) are the 2-D waves

generated in the relaxation zone propagating towards the semi-circular slope. What we then see in Fig. 14(b)–(d) are the waves becoming steeper and transforming due to the presence of the slope before being damped out of the tank completely. What we can conclude then from this case is that the stabilised model is able to accurately simulate the transformation of propagating waves that occurs due to interaction with changing bottom topography, as well as capturing the ensuing three-dimensional nonlinear wave effects. Again, this is all without using numerical damping and without the appearance of the sawtooth instability.

4.4. Energy considerations

As mentioned in the introduction, the use of artificial dissipation by way of a low-order numerical damping or smoothing scheme in FNPF models is undesirable due to overall loss in energy in the NWT. This in turn can then make the models inaccurate, particularly for large-scale and long-time simulations. In addition, this technique usually involves certain parameters that have to be tuned for any given application in order to achieve an optimal balance between stability and accuracy, leading to a very sluggish and drawn-out process if the values are not known a priori. These clear disadvantages of artificial dissipation are at the heart of why we chose to instead make use of a second-order TVD method. Indeed, the stabilised model requires no tuning of any parameters—every preceding validation test case was carried out using the same coding configuration. This is in contrast to the Lin et al. (2021) model for which carefully chosen values of the damping parameters were required to ensure stability and good accuracy. If instead these parameters were poorly chosen, the simulation would have either been unstable, or there would have been excessive damping and overall loss in energy. The stabilised model avoids the process of trial and error in pursuing the optimal damping parameter, so in this sense, it is reasonable to conclude that it is superior to the Lin et al. (2021) model. Nevertheless, to validate this conclusion further, we consider new examples in which we also prove the stabilised model is superior to Lin et al. (2021) model in terms of energy conservation as well.

The most straightforward and heuristic way of verifying the loss in energy due to artificial dissipation is to observe the growing reduction in amplitude of progressive waves as they get further from the inlet. In addition, we can also explicitly calculate the total energy E_T in the NWT over time and see how this corresponds with the prior observations. To calculate E_T, we first calculate the total kinetic and potential energies in the NWT and take their sum, i.e.,

$$E_T = E_k + E_p.$$

(32)

Then, if 0 and X denote the limits of the computational domain in the x-direction and ρ_w is the density of water, E_k and E_p are given by

$$E_k = \frac{1}{2}\rho_w \int_0^X \int_{-h}^{\eta} (\nabla\phi \cdot \nabla\phi)\, dy dx \quad \text{and} \quad E_p = \rho_w g \int_0^X \int_{-h}^{\eta} y\, dy dx,$$

(33)
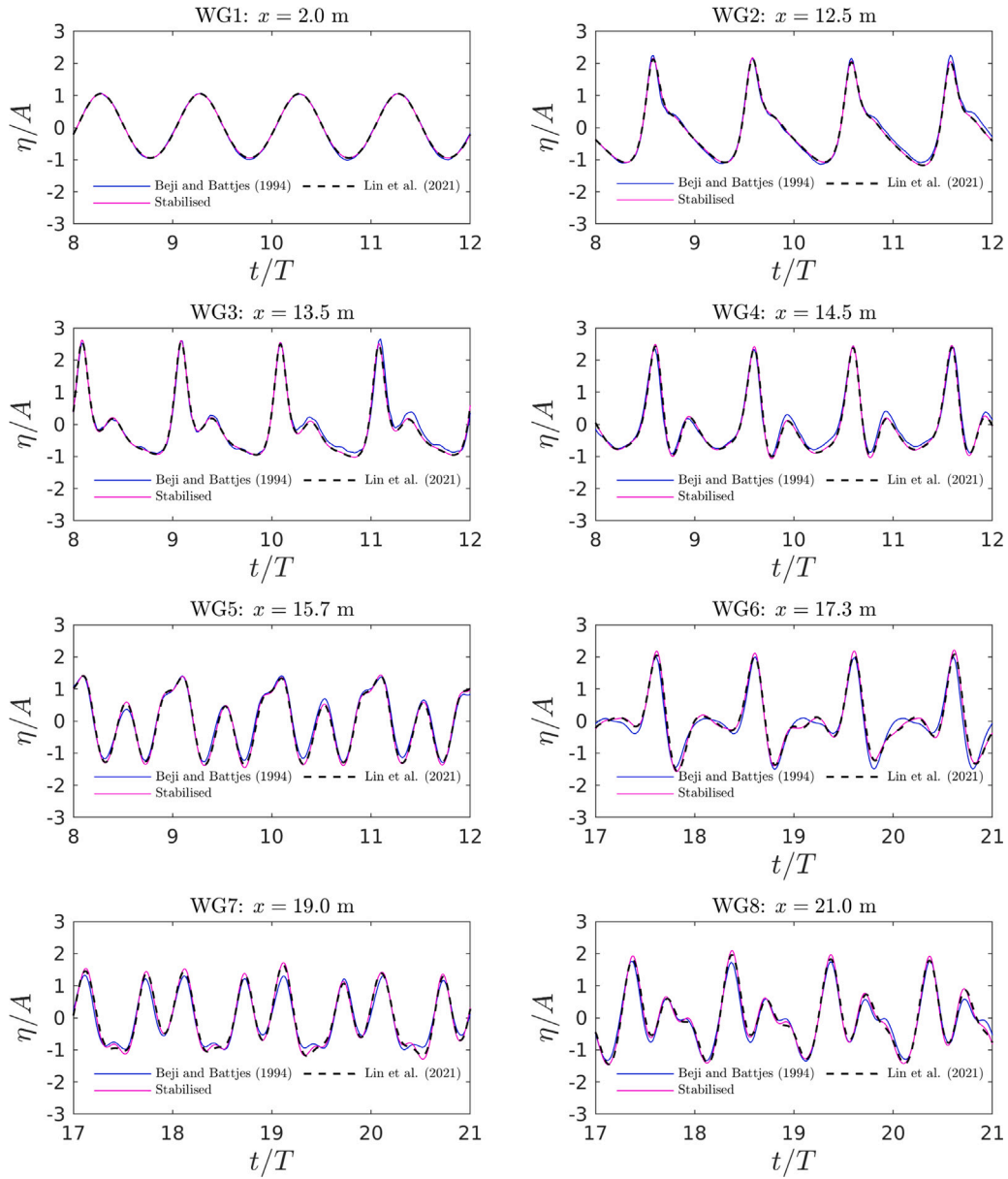
Fig. 10. Time histories of free-surface elevation for the stabilised model, Lin et al. (2021) model, and experimental solution of Beji and Battjes (1994) at various wave gauges in the NWT for input B1.

which in turn implies that

$$E_T = \frac{1}{2}\rho_w \int_0^X \int_{-h}^{\eta} (\nabla\phi \cdot \nabla\phi)\, dy\, dx \; + \; \frac{1}{2}\rho_w g \int_0^X (\eta^2 - h^2)dx. \tag{34}$$

The potential energy below the initial free-surface position $y = 0$, given by $-\frac{1}{2}\rho_w g \int_0^X h^2\, dx$, is a constant that will be the same for each of the two models, and hence is discarded from the calculation for E_T as it has no relation to the wave motion. The total wave energy E_T then becomes

$$E_T = \frac{1}{2}\rho_w \int_0^X \left(\int_{-h}^{\eta} (\nabla\phi \cdot \nabla\phi)\, dy \; + \; g\eta^2 \right) dx. \tag{35}$$

Given that OpenFOAM implements a cell-centred and co-located FVM, calculating the total Energy is relatively straightforward, i.e.,

$$E_T = \frac{1}{2}\rho_w \left(\sum_n^N (\nabla\phi_n \cdot \nabla\phi_n)\, A_n + g \sum_i^I y_i^2 \Delta x_i \right), \tag{36}$$

where N is the total number of mesh cells, A_n the vertical cross-sectional area of cell n, I the number of cells in the x-direction, Δx_i the x-directional width of free-surface cell face i, and y_i the y-coordinate of face i.

Given that we want to consider a large-scale and long-time simulation, we extend the fifth-order Stokes wave example in Section 4.1.2 so that the NWT in this case is 100 wavelengths long with a final time of 450 s. We also change the example to 2D for computational ease. All wave parameters are the same as in Section 4.1.2 (listed in Table 3) meaning the NWT now has dimensions 462 m × 0.7 m. In addition, the relaxation and damping zones are both 5 wavelengths long. The mesh configuration is 5000 × 30 (50 cells per λ). We use the same value of the damping parameter $\beta_{FODC} = 0.05$ with a frequency of every 5 time steps which were found to be optimal for stability. Finally, we split the total energy E_T by considering two separate regions of the NWT: the damping zone (E_D) and the 'middle portion' (E_M) which is the region
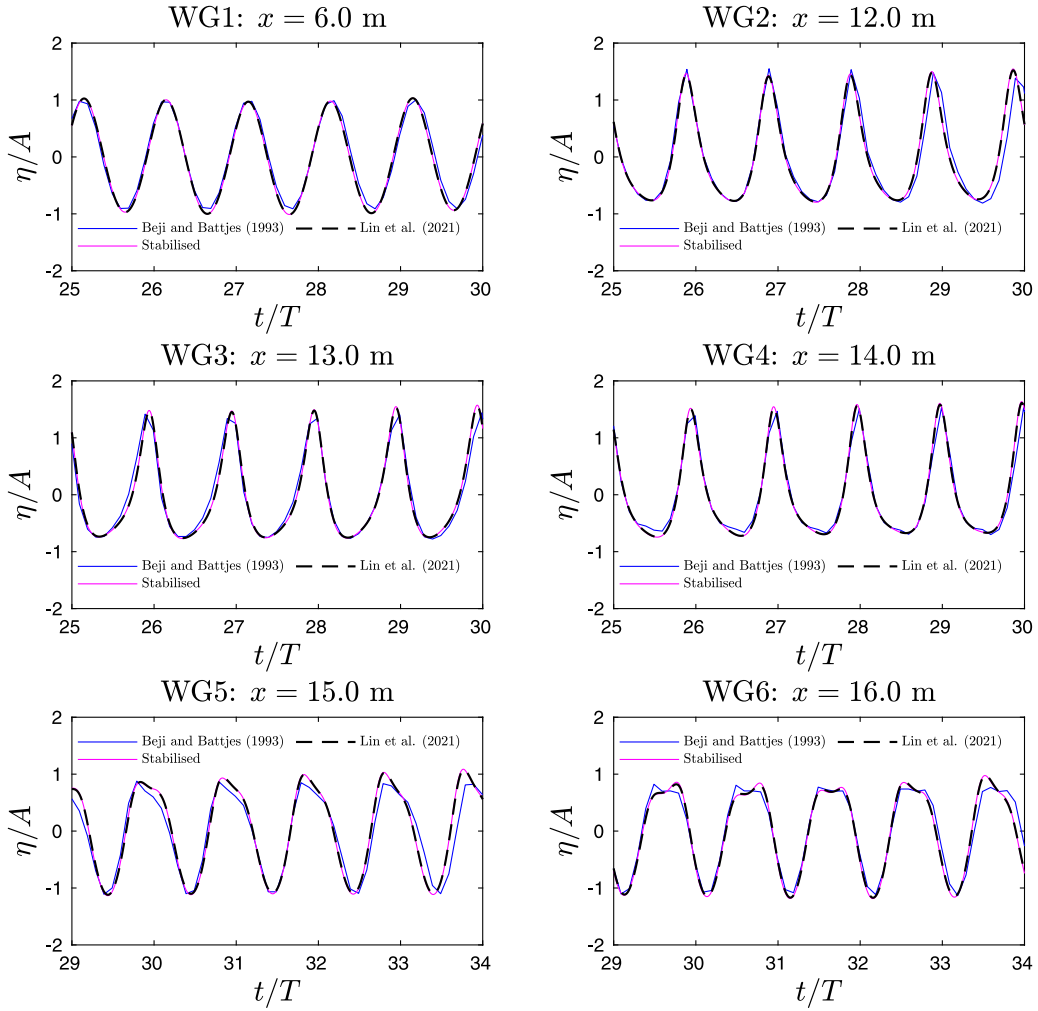
Fig. 11. Time histories of free-surface elevation for the stabilised model, Lin et al. (2021) model, and experimental solution of Beji and Battjes (1993) at various wave gauges in the NWT for input B2.

Fig. 12. Illustration of submerged semi-circular slope for 3-D shoaling case.

that does not include both the relaxation and damping zones (and is hence 90 wavelengths long).

Fig. 15(a) then shows the time histories of free-surface elevation for the stabilised model, Lin et al. (2021) model, and analytical fifth-order Stokes solution at WG1 = 430 m. Note this wave gauge is near the end of the NWT, just before the damping zone begins. We can

see from the results that the Lin et al. (2021) model experiences a greater reduction in amplitude – and hence a greater loss in energy – of propagating waves than the stabilised model. Although the stabilised model also experiences a reduction in amplitude, the loss is smaller than the Lin et al. (2021) model; hence, in this sense, the new model outperforms the old one. The results when we explicitly calculate the energy are also in agreement with this heuristic observation. Fig. 15(b) shows the time histories of E_D for the stabilised model and Lin et al. (2021) model in the damping zone of the NWT. These results clearly show that the amount of energy having to be transferred out of the NWT in this zone is higher for the stabilised model than the Lin et al. (2021) model, clearly indicating that the waves in the stabilised model are propagating more energy at the point which they reach the damping zone for all time—a result corroborated by the results in Fig. 15(a). In addition, Fig. 15(c) shows analogous results for E_M in the middle portion of the NWT where waves are not being generated or damped but only propagated. It clearly shows that the stabilised model conserves more energy over time than the Lin et al. (2021) model. According to Dong et al. (2020), the theoretical total wave energy per unit horizontal area for this fifth-order Stokes wave in the middle portion of the NWT can be found at about $\overline{E} = 75.9$ J/m². The corresponding computed values are 65.4 J/m² and 60.9 J/m² for the stabilised and old models, respectively. These energy calculations clearly corroborate our prior heuristic observations and hence further cement the superiority of the stabilised model over the Lin et al. (2021)
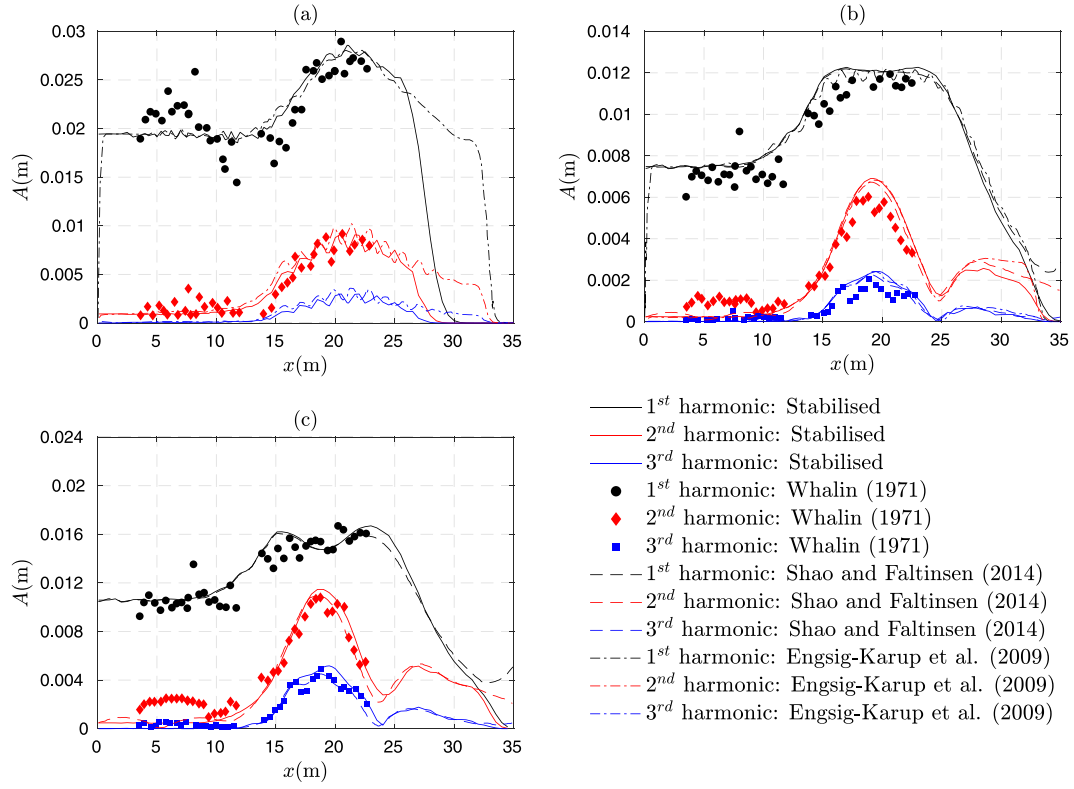
Fig. 13. Harmonic components of numerical results from the stabilised model, Shao and Faltinsen (2014), Engsig-Karup et al. (2009), and experimental results of Whalin (1971) at the streamwise central line of the NWT: (a.) input W1, (b.) input W2, (c.) input W3.
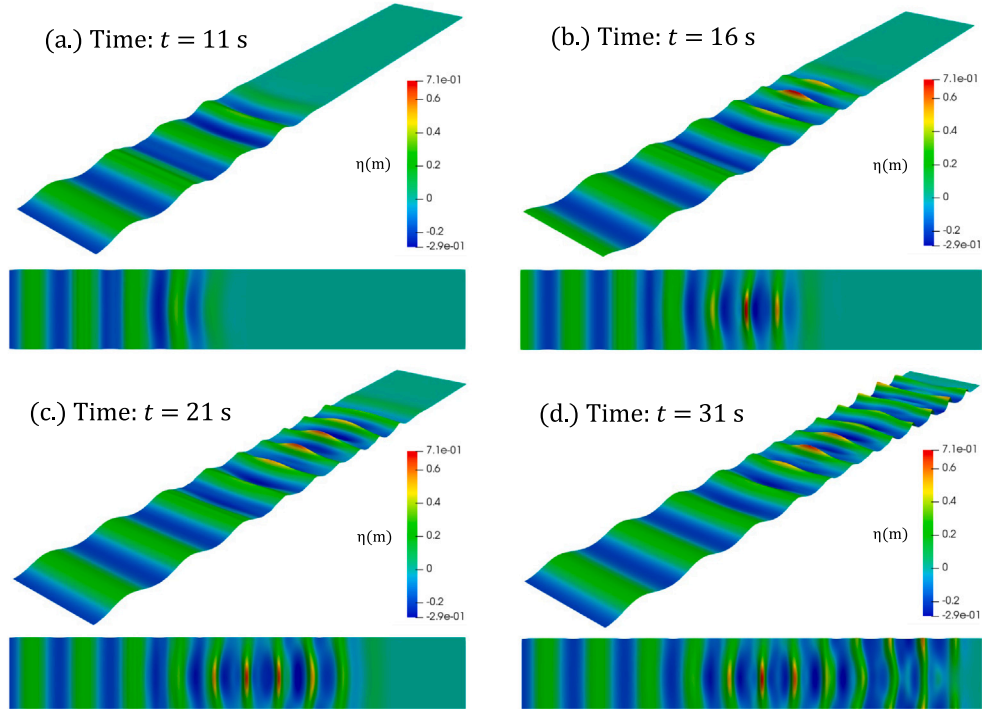

Fig. 14. Snapshots of the free surface for input W3 at times (a.) 11 s, (b.) 16 s, (c.) 21 s, and (d.) 31 s. (Not to scale—exaggerated 20 times in the *y*-direction).
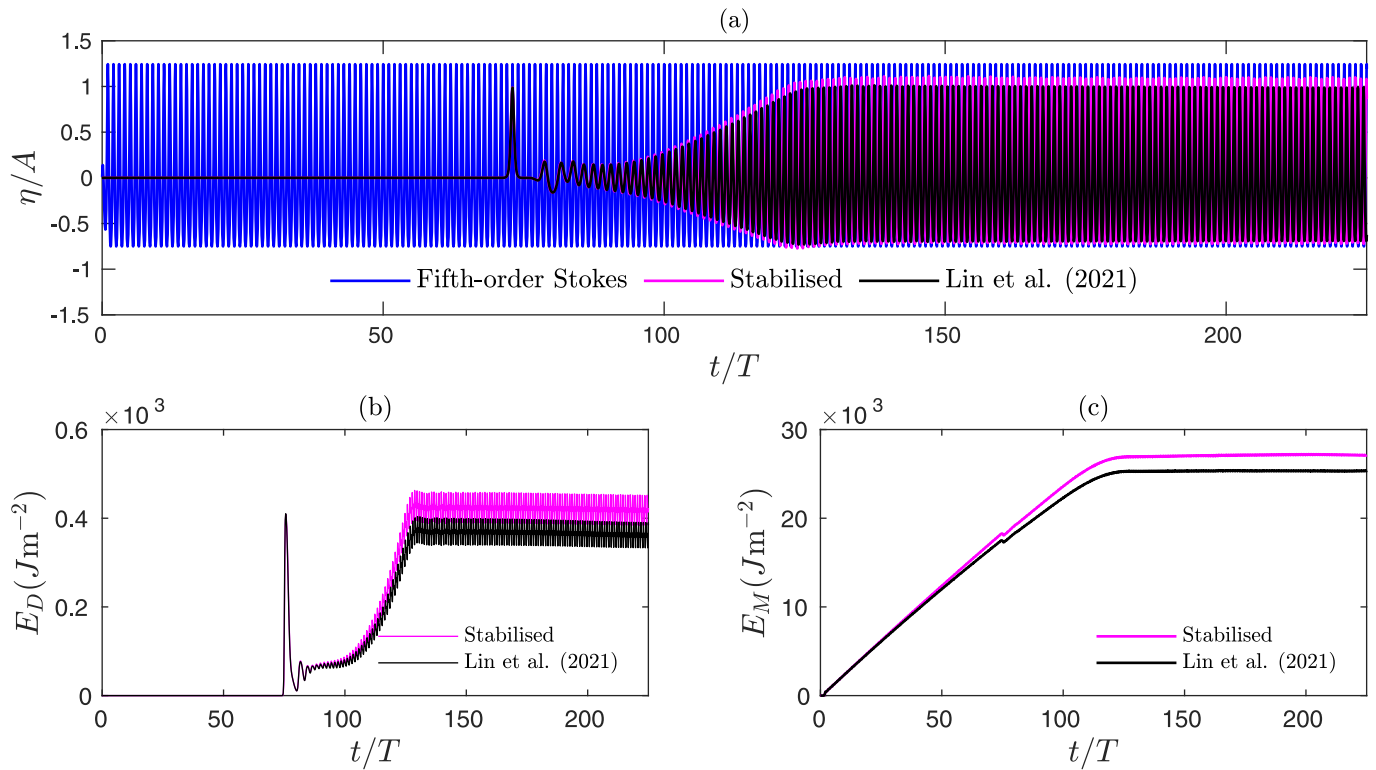
Fig. 15. (a.) Time histories of free-surface elevation for the stabilised model, Lin et al. (2021) model, and fifth-order Stokes solution at WG1 = 430 m. (b.) Time histories of total energy E_D in the damping zone of the NWT for the stabilised model and Lin et al. (2021) model. (c.) Time histories of total energy E_M in the middle portion of the NWT for the stabilised model and Lin et al. (2021) model.

model in terms of energy conservation and accuracy for large-scale and long-time simulations.

5. Conclusion

In the present paper, we have endeavoured to stabilise the finite volume model of Lin et al. (2021) without resorting to the different types of filters that are often used in FNPF models. We did this by first analysing the characteristics of the nonlinear boundary condition equations. This showed that the KBC equation is advection dominated, meaning that the advection terms in it need to be handled correctly. In order to stabilise numerical simulations and avoid the use of undesirable techniques that involve artificial dissipation, we proposed a new method to calculate the advection terms in the KBC equation; namely, a second-order scheme motivated by a TVD approach.

It was found that this eliminated the instability in every instance for which it occurred in the original Lin et al. (2021) model. Furthermore, we demonstrated through a variety of validation test cases that the stabilised model is accurate, with good agreements being shown with existing numerical, experimental, and analytical results. This was particularly evident when evaluating the performance in terms of energy conservation; indeed, we showed that the stabilised model is much better suited to large-scale and long-time simulations than the Lin et al. (2021) model—vindicating the desire to be free from using numerical damping as a stabilisation technique. We also highlighted the simplicity and ease as to which the TVD method could be implemented and used in existing finite volume-based FNPF models. In addition, the speed and efficiency of the stabilised model is on par with the Lin et al. (2021) model.

It should be noted that, for time integration, we only used the first-order Euler scheme as Lin et al. (2021) did. This was solely for the purpose of fair comparison between the two models in terms of their performance. Higher-order time integration schemes will be used in

future work. Finally, as mentioned in the introduction, our primary aim is to use this new stabilised model as a constituent part for a new robust and efficient integrated model. We plan to do this by coupling it with the native two-phase Navier–Stokes solver readily available in OpenFOAM, something for which this FNPF model has an advantage given that it too has been developed in OpenFOAM and is finite volume based. This new multi-scale integrated NWT will then be used to model complex wave–structure interactions to high level of efficiency and accuracy.

CRediT authorship contribution statement

Ranjodh Rai: Methodology, Software, Writing – original draft. **Zhihua Ma:** Conceptualization, Methodology, Software, Writing – original draft. **Zaibin Lin:** Data curation, Methodology. **Wei Bai:** Methodology. **Ling Qian:** Conceptualization.

Declaration of competing interest

The authors declare the following financial interests/personal relationships which may be considered as potential competing interests: Zhihua Ma reports financial support was provided by Engineering and Physical Sciences Research Council. Ling Qian reports financial support was provided by Engineering and Physical Sciences Research Council. Co-author Dr Wei Bai is an Editorial Board member of the journal.

Data availability

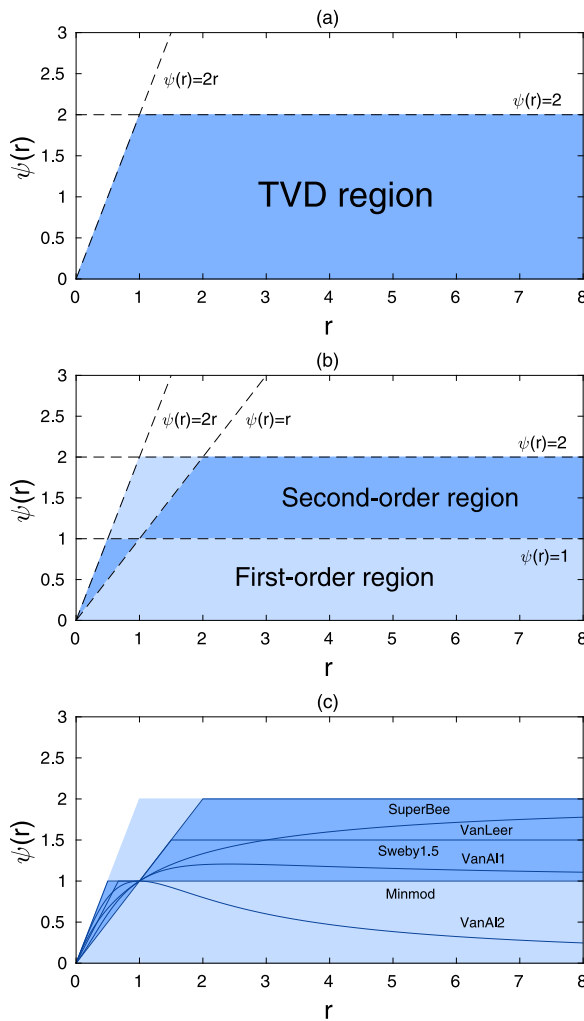Data will be made available on request.

Fig. 16. (a) TVD region for the flux limiter function $\psi(r)$, (b) First and second-order regions, (c) Popular functions.

Table 10
Expressions for some popular flux limiter functions.

Limiter	$\psi(r)$
Van Leer	$\dfrac{r+\lvert r\rvert}{1+\lvert r\rvert}$
Van Albada 1	$\dfrac{r^2+r}{r^2+1}$
Van Albada 2	$\dfrac{2r}{r^2+1}$
MinMod	$\max[0,\ \min(1,\ r)]$
SuperBee	$\max[0,\ \min(1,\ 2r),\ \min(2,\ r)]$
Sweby	$\max[0,\ \min(1,\ \beta r),\ \min(\beta,\ r)]$

- If $0 < r < 1$, the upper limit is $\psi(r) = 2r$, so for TVD schemes $\psi(r) \leq 2r$.
- If $r \geq 1$, the upper limit is $\psi(r) = 2$, so for TVD schemes $\psi(r) \leq 2$.

These constraints result in the TVD region visualised in Fig. 16(a). From this we can conclude that the key to ensuring that the numerical scheme is TVD is to construct a flux limiter function $\psi(r)$ that remains in this region for all r. Moreover, Sweby also deduced that the choice of $\psi(r)$ dictates the order of the scheme. For a scheme to be second order, $\psi(r)$ must satisfy further constraints:

- If $0 < r < 1$, the lower limit is $\psi(r) = r$, the upper limit is $\psi(r) = 1$, so for TVD schemes $r < \psi(r) < 1$.
- If $r \geq 1$, the lower limit is $\psi(r) = 1$, the upper limit is $\psi(r) = r$, so for TVD schemes $1 \leq \psi(r) \leq r$.
- $\psi(r)$ must pass through the point $(1, 1)$ in the $r - \psi(r)$ diagram.

These additional constraints result in a partition of the larger TVD region into separate second and first-order regions, as shown in Fig. 16(b). Fig. 16(c) then shows some popular flux limiter functions plotted on a $r-\psi(r)$ diagram, with the corresponding expressions shown in Table 10.

References

Beji, S., Battjes, J., 1993. Experimental investigation of wave propagation over a bar. Coast. Eng. 19, 151–162.

Beji, S., Battjes, J., 1994. Numerical simulation of nonlinear wave propagation over a bar. Coast. Eng. 23, 1–16.

Bihs, H., Chella, M., Kamath, A., Arntsen, Ø., 2017. Numerical investigation of focused waves and their interaction with a vertical cylinder using reef3d. J. Offshore Mech. Arct. Eng. 139.

Bihs, H., Wang, W., Pâkozdi, C., Kamath, A., 2020. Reef3d::fnpf - a flexible fully nonlinear potential flow solver. J. Offshore Mech. Arct. Eng. 142, 1–12.

Dias, F., Bridges, T., 2006. The numerical computation of freely propagating time-dependent irrotational water waves. Fluid Dyn. Res. 38, 803–830.

Dold, J., 1992. An efficient surface-integral algorithm applied to unsteady gravity waves. J. Comput. Phys. 103, 90–115.

Dold, J., Peregrine, D., 1986. An efficient boundary integral method for steep unsteady water waves. In: Numerical Methods for Fluid Dynamics II. Oxford University Press, pp. 671–679.

Dong, G., Gao, X., Ma, X., Ma, Y., 2020. Energy properties of regular water waves over horizontal bottom with increasing nonlinearity. Ocean Eng. 218, 108159.

Ducrozet, G., Bonnefoy, F., Le Touzé, D., Ferrant, P., 2016. Hos-ocean: Open-source solver for nonlinear waves in open ocean based on high-order spectral method. Comput. Phys. Comm. 203, 245–254.

Engsig-Karup, A., Bingham, H., Lindberg, O., 2009. An efficient flexible-order model for 3d nonlinear water waves. J. Comput. Phys. 228, 2100–2118.

Engsig-Karup, A., Eskilsson, C., Bigoni, D., 2016. A stabilised nodal spectral element method for fully nonlinear water waves. J. Comput. Phys. 318, 1–21.

Ferrand, M., Harris, J., 2021. Finite volume arbitrary lagrangian-eulerian schemes using dual meshes for ocean wave applications. Comput. & Fluids 219, 104860.

Fructus, D., Clamond, D., Grue, J., Kristiansen, O., 2005. An efficient model for three-dimensional surface wave simulations: Part i: Free space problems. J. Comput. Phys. 205, 665–685.

Grilli, S., Guyenne, P., Dias, F., 2001. A fully non-linear model for three-dimensional overturning waves over an arbitrary bottom. Internat. J. Numer. Methods Fluids 35, 829–867.

Grilli, S., Skourup, J., Svendsen, I., 1989. An efficient boundary element method for nonlinear water waves. Eng. Anal. Bound. Elem. 6, 97–107.

Hanssen, F., Helmers, J., Greco, M., Shao, Y., 2022. A 3d fully-nonlinear potential-flow solver for efficient simulations of large-scale free-surface waves. Internat. J. Numer. Methods Engrg..

Harten, A., 1983. High resolution schemes for hyperbolic conservation laws. J. Comput. Phys. 49, 357–393.

Kim, M., Celebi, M., Kim, D., 1998. Fully nonlinear interactions of waves with a three-dimensional body in uniform currents. Appl. Ocean Res. 20, 309–321.

Li, B., Fleming, C., 1997. A three dimensional multigrid model for fully nonlinear water waves. Coast. Eng. 30, 235–258.

Lin, Z., Qian, L., Bai, W., Ma, Z., Chen, H., Zhou, J., Gu, H., 2021. A finite volume based fully nonlinear potential flow model for water wave problems. Appl. Ocean Res. 106, 102445.

Longuet-Higgins, M., Cokelet, E., 1976. The deformation of steep surface waves on water-i. A numerical method of computation. Proc. R. Soc. Lond. Ser. A Math. Phys. Eng. Sci. 350, 1–26.

Appendix. Flux limiter

Constraints by Sweby (1984):

Ma, Q., Wu, G., Eatock Taylor, R., 2001a. Finite element simulation of fully non-linear interaction between vertical cylinders and steep waves. part 1: methodology and numerical procedure. Internat. J. Numer. Methods Fluids 36, 265–285.

Ma, Q., Wu, G., Eatock Taylor, R., 2001b. Finite element simulations of fully non-linear interaction between vertical cylinders and steep waves. part 2: numerical results and validation. Internat. J. Numer. Methods Fluids 36, 287–308.

Ma, Q., Yan, S., 2006. Quasi ale finite element method for nonlinear water waves. J. Comput. Phys. 212, 52–72.

Ma, Q., Yan, S., 2009. Qale-fem for numerical modelling of non-linear interaction between 3d moored floating bodies and steep waves. Internat. J. Numer. Methods Engrg. 78, 713–756.

Mayer, S., Garapon, A., Sørensen, L., 1998. A fractional step method for unsteady free-surface flow with applications to non-linear wave dynamics. Internat. J. Numer. Methods Fluids 28, 293–315.

Mehmood, A., Graham, D., Langfeld, K., Greaves, D., 2016. Numerical simulation of nonlinear water waves based on fully nonlinear potential flow theory in openfoam-extend. In: Proceedings of the Twenty-Sixth (2016) International Ocean and Polar Engineering Conference. International Society of Offshore and Polar Engineers.

Mola, A., Heltai, L., DeSimone, A., 2013. A stable and adaptive semi-lagrangian potential model for unsteady and nonlinear ship-wave interactions. Eng. Anal. Bound. Elem. 37, 128–143.

Ning, D., Teng, B., Eatock Taylor, R., Zang, J., 2008. Numerical simulation of non-linear regular and focused waves in an infinite water-depth. Ocean Eng. 35, 887–899.

Ning, D., Zang, J., Liu, S., Eatock Taylor, R., Teng, B., Taylor, P., 2009. Free-surface evolution and wave kinematics for nonlinear uni-directional focused wave groups. Ocean Eng. 36, 1226–1243.

Savitzky, A., Golay, M., 1964. Smoothing and differentiation of data by simplified least squares procedures. Anal. Chem. 36, 1627–1639.

Shao, Y., Faltinsen, O., 2014. A harmonic polynomial cell (hpc) method for 3d laplace equation with application in marine hydrodynamics. J. Comput. Phys. 274, 312–332.

Shao, Y., Zheng, Z., Liang, H., Chen, J., 2022. A consistent second-order hydrodynamic model in the time domain for floating structures with large horizontal motions. Comput.-Aided Civ. Infrastruct. Eng..

Sweby, P., 1984. High resolution schemes using flux limiters for hyperbolic conservation laws. SIAM J. Numer. Anal. 21, 995–1011.

Wang, W., Kamath, A., Pakozdi, C., Bihs, H., 2019. Investigation of focusing wave properties in a numerical wave tank with a fully nonlinear potential flow model. J. Mar. Sci. Eng. 7, 375.

Westphalen, J., Greaves, D., Williams, C., Hunt-Raby, A., Zang, J., 2012. Focused waves and wave–structure interaction in a numerical wave tank. Ocean Eng. 45, 9–21.

Whalin, R., 1971. The Limit of Applicability of Linear Wave Refraction Theory in a Convergence Zone. Technical Report, Army Engineer Waterways Experiment Station Vicksburg Miss.

Wu, G., Eatock Taylor, R., 1994. Finite element analysis of two-dimensional non-linear transient water waves. Appl. Ocean Res. 16, 363–372.

Yan, S., Ma, Q., 2007. Numerical simulation of fully nonlinear interaction between steep waves and 2d floating bodies using the qale-fem method. J. Comput. Phys. 221, 666–692.